

# Big-bang nucleosynthesis through bound-state effects with a long-lived slepton in the NMSSM

Kazunori Kohri,<sup>1</sup> Masafumi Koike,<sup>2</sup> Yasufumi Konishi,<sup>3</sup> Shingo Ohta,<sup>3</sup>  
Joe Sato,<sup>3</sup> Takashi Shimomura,<sup>4</sup> Kenichi Sugai,<sup>3</sup> and Masato Yamanaka<sup>5</sup>

<sup>1</sup>*KEK (High Energy Accelerator Research Organization),  
and Sokendai, 1-1 Oho, Tsukuba 305-0801, Japan*

<sup>2</sup>*Department of Information Science, Utsunomiya University, Yoto, Utsunomiya, Tochigi 321-8585, Japan*

<sup>3</sup>*Department of Physics, Saitama University, Shimo-okubo, Sakura-ku, Saitama, 338-8570, Japan*

<sup>4</sup>*Department of Physics, Niigata University, Niigata, 950-2181, Japan*

<sup>5</sup>*Department of Physics, Nagoya University, Nagoya 464-8602, Japan*

We show that the Li problems can be solved in the next-to-minimal supersymmetric standard model where the slepton as the next-to-lightest SUSY particle is very long-lived. Such a long-lived slepton induces exotic nuclear reactions in big-bang nucleosynthesis, and destroys and produces the  ${}^7\text{Li}$  and  ${}^6\text{Li}$  nuclei via bound state formation. We study cases where the lightest SUSY particle is singlino-like neutralino and bino-like neutralino to present allowed regions in the parameter space which is consistent with the observations on the dark matter and the Higgs mass.

## I. INTRODUCTION

The Standard Model has had enormous successes in describing the interactions of the elementary particles, predicting almost every experimental results with accuracy. The recent discovery of the Higgs particle finally crowned the accumulation of successes [1, 2]. On the other hand, it left us a number of questions that suggest the presence of a more fundamental theory behind. Among such questions is the nature of dark matter; it became a compelling question during this decade after the precise observations of the universe reported their results [3, 4]. The theory behind the Standard Model ought to account for this question. Supersymmetric models have been attractive candidates for such theories. The Minimal Supersymmetric Standard Model (MSSM) is the simplest extension and most analyzed. The lightest supersymmetric particle should be neutral and stable, and thus can be the dark matter. Other extensions are also of interest, one of which is the Next-to-Minimal Supersymmetric Standard Model (NMSSM). An extra singlet chiral supermultiplet is introduced in the NMSSM, and thereby account for the  $\mu$ -problem [5] that complicates the MSSM. In addition, the NMSSM better reconciles with the observed Higgs mass of 125 GeV. The MSSM predicts a Higgs mass lighter than that of the  $Z$  boson at the tree level, and employs loop effects to raise it up to the observed value. On the other hand, the Higgs mass in the NMSSM has additional terms contributed from the singlet, and it potentially offers a straightforward interpretation of the observations.

A series of works by the present authors explored impacts of the supersymmetry on the nucleosynthesis in the early universe [6–11]. Focus in these works has been on

the case where the next-to-lightest supersymmetric particle (NLSP) is charged and long-lived so that it survives until the time of nucleosynthesis after the big-bang. It takes part in the nuclear reactions and alters the present-day abundance of the light elements. Possible disagreement indeed persists on the abundance of lithium compared with the calculation based on the standard big-bang nucleosynthesis (BBN) scenario. The standard calculation predicts the ratio of abundance  $\text{Log}_{10}({}^7\text{Li}/\text{H})$  to be  $-9.35 \pm 0.06$  [10], while the observation indicates  $-9.63 \pm 0.06$  [12]. Lithium 6 provides another possible disagreement; its observed ratio of abundance  ${}^6\text{Li}/{}^7\text{Li} = 0.046 \pm 0.022$  is about  $10^2$ – $10^3$  larger than the theoretical prediction [13]. These discrepancies can be the trace of the interaction between nuclei and the NLSP which is absent in the standard BBN scenario. Our scenario can thereby account for the abundance of the dark matter and of the lithium in a single framework. We analyzed if this scenario works within the MSSM with staus as the NLSP and neutralinos as the lightest supersymmetric particle (LSP), and found the parameter region that can account for these observational handles to the new physics [6–10].

Now that the mass of Higgs particle is determined, we are to examine whether it is compatible with our scenario. Our previous work analyzed the constrained minimal supersymmetric standard model [14]. There we found allowed regions in the parameter space, and presented phenomenological predictions such as mass spectra and branching ratios. In the present paper, we further extend our scenario to the NMSSM with the flavor violation and search for its further applications. We demonstrate that the NMSSM under our scenario can simultaneously account for the three phenomenological clues: the abundance of dark matter, that of lithium, and Higgs

mass. We explore parameter space and discover parameter points that qualify the requirements. Special interest is in the case where the NMSSM singlet is the major component of the neutralino LSP in expectation of the difference from the MSSM. The case of bino-like neutralino is analyzed as well.

This paper is organized as follows. In Sec. II, we introduce the NMSSM and define the model of our interest. The BBN in the presence of a long-lived slepton is also explained in this section. The exotic reactions that are absent from the standard BBN are introduced. Section III describes our strategy to find out the parameter point that are consistent with the three phenomenological clues. The results are presented in Sec. IV. We show the three benchmark cases characterized by the type of neutralino LSP. The first case considers singlino-like neutralinos. The couplings of the singlet is small and  $\tan\beta$  is large in this case. The second case also handles singlino-like neutralinos, but the singlet couplings are large and  $\tan\beta$  is small compared with the first case. The third case deals with bino-like neutralinos. Singlet couplings are set large and  $\tan\beta$  small as in the second case. We show that each of these three cases allows the phenomenological constraints. We spot benchmark points in the parameter space and exhibit that they accord with the observations. The NMSSM parameters are calculated to confirm the adequate Higgs mass, and the BBN network calculation is carried out to check the relic abundance of light elements and of the LSP dark matter. The present work is summarized in Sec. V.

## II. THE NMSSM AND THE EXOTIC BBN

We recapitulate the Higgs and neutralino sectors, and explain exotic BBN processes with a long-lived slepton in the NMSSM.

### A. Higgs bosons

The NMSSM specific part of the superpotential and the soft-breaking terms are

$$W^{\text{NMSSM}} \supset \lambda \hat{S} \hat{H}_d \cdot \hat{H}_u + \frac{1}{3} \kappa \hat{S}^3, \quad (1)$$

$$-\mathcal{L}_{\text{soft}}^{\text{NMSSM}} \supset m_{\hat{S}}^2 |S|^2 + \left( \lambda A_\lambda H_d \cdot H_u S + \frac{1}{3} \kappa A_\kappa S^3 + \text{h.c.} \right), \quad (2)$$

where  $\mathcal{Z}_3$  parity conservation is assumed. In Eq. (1),  $\hat{H}_d$ ,  $\hat{H}_u$  and  $\hat{S}$  are the Higgs superfields and the singlet superfield. The couplings  $\lambda$  and  $\kappa$  are dimensionless parameters. In Eq. (2),

$$H_d = \begin{pmatrix} H_d^0 \\ H_d^- \end{pmatrix}, \quad H_u = \begin{pmatrix} H_u^+ \\ H_u^0 \end{pmatrix}, \quad S \quad (3)$$

are two Higgs doublets and a singlet scalar. We denote vacuum expectation values of their neutral components by  $v_d$ ,  $v_u$ , and  $s$ , respectively. The soft-breaking parameters are  $m_S$ ,  $A_\lambda$  and  $A_\kappa$ . The free parameters in the Higgs sector are  $\lambda$ ,  $\kappa$ ,  $A_\lambda$ ,  $A_\kappa$ ,  $\tan\beta$  ( $\equiv v_u/v_d$ ), and  $\mu_{\text{eff}}$  ( $\equiv \lambda s$ ).

The Higgs mass up to dominant 1-loop contribution is

$$m_h^2 = m_Z^2 \cos^2 2\beta + \lambda^2 v^2 \sin^2 2\beta - \frac{\lambda^2}{\kappa^2} v^2 (\lambda - \kappa \sin 2\beta)^2 + \frac{3m_t^2}{16\pi^2 v^2} \left\{ \log \left( \frac{m_s^2}{m_t^2} \right) + \frac{X_t^2}{m_s^2} \left( 1 - \frac{X_t^2}{12m_s^2} \right) \right\}, \quad (4)$$

where  $m_Z$  is  $Z$  boson mass,  $m_t$  is the top mass,  $m_s \equiv \sqrt{m_{\tilde{t}_1} m_{\tilde{t}_2}}$  is geometric mean of stop masses,  $X_t = A_t - \mu_{\text{eff}} \cot\beta$ , and  $v = \sqrt{v_d^2 + v_u^2} = 174$  GeV. The second and third tree terms are characteristic in the NMSSM, and can lift up the Higgs mass. This is one of the attractive features of the model. In contrast, significant 1-loop contribution (the last term in Eq. (4)) is required to obtain the Higgs mass around 125 GeV in the MSSM since the tree contribution is at most  $m_Z$ . The 1-loop contribution is maximized by the relation,  $X_t = \sqrt{6}m_s$ , with large stop mass scale. In the NMSSM we do not need to rely on such conditions to obtain observed Higgs mass.

### B. Neutralinos

In the NMSSM the neutralinos are linear combinations of bino  $\tilde{B}$ , wino  $\tilde{W}$ , neutral higgsinos  $\tilde{H}_d^0$  and  $\tilde{H}_u^0$ , and singlino  $\tilde{S}$ , the supersymmetric partner of the singlet scalar:

$$\tilde{\chi}_i^0 = N_{i\tilde{B}} \tilde{B} + N_{i\tilde{W}} \tilde{W} + N_{i\tilde{H}_d^0} \tilde{H}_d^0 + N_{i\tilde{H}_u^0} \tilde{H}_u^0 + N_{i\tilde{S}} \tilde{S}, \quad (5)$$

where  $i$  runs from 1 to 5. The mass matrix of the neutralinos is given by the following symmetric expression in the basis  $(\tilde{B}, \tilde{W}, \tilde{H}_d^0, \tilde{H}_u^0, \tilde{S})$ :

$$\mathcal{M}_{\tilde{\chi}^0} = \begin{pmatrix} M_1 & 0 & -c_\beta s_W m_Z & s_\beta s_W m_Z & 0 \\ & M_2 & c_\beta c_W m_Z & -s_\beta c_W m_Z & 0 \\ & & 0 & -\mu_{\text{eff}} & -\mu_\lambda s_\beta \\ & & & 0 & -\mu_\lambda c_\beta \\ & & & & \mu_\kappa \end{pmatrix}, \quad (6)$$

where  $M_1$  and  $M_2$  are masses of the gauginos,  $c_\beta = \cos\beta$ ,  $s_\beta = \sin\beta$ ,  $c_W = \cos\theta_W$ ,  $s_W = \sin\theta_W$ ,  $\mu_\lambda = \lambda v$ , and  $\mu_\kappa = 2\kappa s$ . Here  $\theta_W$  is the Weinberg angle. We consider the case where the LSP is the lightest neutralino,  $\tilde{\chi}_1^0$ , and the NLSP is the lightest slepton,  $\tilde{l}$ .

As we will see later, the interaction among  $\tilde{\chi}_1^0$ ,  $\tilde{l}$ , and a lepton  $f$  is a key ingredient in this study. The interaction Lagrangian is written as

$$-\mathcal{L}_{\tilde{\chi}_1^0-f-\tilde{l}} = \tilde{l}^* \tilde{\chi}_1^0 (G_{Lf} P_L + G_{Rf} P_R) f + \text{h.c.}, \quad (7)$$

where

$$G_{Lf} = c_f \left[ \frac{g_2}{\sqrt{2}} \cos \theta_f (\tan \theta_W N_{1\tilde{B}} + N_{1\tilde{W}}) - \frac{m_f g_2}{\sqrt{2} m_W \cos \beta} \sin \theta_f N_{1\tilde{H}_d^0} \right], \quad (8)$$

$$G_{Rf} = c_f \left[ \sqrt{2} g_2 \sin \theta_f \tan \theta_W N_{1\tilde{B}} + \frac{m_f g_2}{\sqrt{2} m_W \cos \beta} \cos \theta_f N_{1\tilde{H}_d^0} \right]. \quad (9)$$

Here  $g_2$  is the gauge coupling constant of SU(2),  $m_f$  is the mass of the lepton  $f$ , and  $f = e, \mu$ , and  $\tau$ . The slepton is expanded as a linear combination of the flavor eigenstates:

$$\tilde{l} = \sum_{f=e,\mu,\tau} c_f \tilde{f}, \quad \tilde{f} = \cos \theta_f \tilde{f}_L + \sin \theta_f \tilde{f}_R, \quad (10)$$

where  $\tilde{f}_L$  and  $\tilde{f}_R$  are the flavor eigenstates, and the coefficients are normalized as  $c_e^2 + c_\mu^2 + c_\tau^2 = 1$ . Hereafter we assume that  $\sin \theta_e = \sin \theta_\mu = \sin \theta_\tau$  and no CP-violating phase exists in the slepton sector.

We study two scenarios where the lightest neutralino is singlino- and bino-like. The detailed expressions of  $\tilde{\chi}_1^0$  and the couplings  $G_{Lf}$  and  $G_{Rf}$  are different between the two cases. In the followings, we explicitly write down the mixing of the lightest neutralino in each case up to the second order in perturbation theory.

### 1. Singlino-like neutralino LSP

Up to the second order perturbative expansion, the singlino-like neutralino is

$$\begin{aligned} \tilde{\chi}^0 = & - \frac{m_Z \mu_{\text{eff}} \mu_\lambda s_W c_{2\beta}}{(\mu_\kappa - M_1)(\mu_\kappa^2 - \mu_{\text{eff}}^2)} \tilde{B} \\ & + \frac{m_Z \mu_{\text{eff}} \mu_\lambda c_W c_{2\beta}}{(\mu_\kappa - M_2)(\mu_\kappa^2 - \mu_{\text{eff}}^2)} \tilde{W} \\ & + \frac{\mu_\lambda (\mu_{\text{eff}} c_\beta - \mu_\kappa s_\beta)}{\mu_\kappa^2 - \mu_{\text{eff}}^2} \tilde{H}_d^0 \\ & + \frac{\mu_\lambda (\mu_{\text{eff}} s_\beta - \mu_\kappa c_\beta)}{\mu_\kappa^2 - \mu_{\text{eff}}^2} \tilde{H}_u^0 \\ & + \tilde{S}, \end{aligned} \quad (11)$$

where  $c_{2\beta} = \cos 2\beta$ , and the normalization factor is omitted. If the neutralino Eq. (11) is the LSP, the mixings  $N_{1\tilde{B}}, N_{1\tilde{W}}$  and  $N_{1\tilde{H}_d^0}$  in Eqs. (8) and (9) can be read off by comparing Eqs. (5) and (11). The free parameters in  $G_{Lf}$  and  $G_{Rf}$  are  $M_1, M_2, \lambda, \kappa, \tan \beta, c_f$ , and  $\theta_f$ .

### 2. Bino-like neutralino LSP

Up to the second order perturbative expansion, the bino-like neutralino is

$$\begin{aligned} \tilde{\chi}^0 = & \tilde{B} \\ & - \frac{m_Z^2 s_W c_W (M_1 + \mu_{\text{eff}} s_{2\beta})}{(M_1 - M_2)(M_1^2 - \mu_{\text{eff}}^2)} \tilde{W} \\ & - \frac{m_Z s_W (M_1 c_\beta + \mu_{\text{eff}} s_\beta)}{M_1^2 - \mu_{\text{eff}}^2} \tilde{H}_d^0 \\ & + \frac{m_Z s_W (M_1 s_\beta + \mu_{\text{eff}} c_\beta)}{M_1^2 - \mu_{\text{eff}}^2} \tilde{H}_u^0 \\ & - \frac{m_Z \mu_{\text{eff}} \mu_\lambda s_W c_{2\beta}}{(M_1 - \mu_\kappa)(M_1^2 - \mu_{\text{eff}}^2)} \tilde{S}, \end{aligned} \quad (12)$$

where  $s_{2\beta} = \sin 2\beta$ , and the normalization factor is omitted. If the neutralino Eq. (12) is the LSP, the mixings  $N_{1\tilde{B}}, N_{1\tilde{W}}$  and  $N_{1\tilde{H}_d^0}$  in Eqs. (8) and (9) can be read off by comparing Eqs. (5) and (12). The free parameters in  $G_{Lf}$  and  $G_{Rf}$  are  $M_1, M_2, \lambda, \tan \beta, \mu_{\text{eff}}, c_f$ , and  $\theta_f$ . The couplings do not depend on  $\kappa$ .

### C. BBN with a long-lived slepton

We explain exotic BBN processes caused by a long-lived slepton. Then we explain the difference of the couplings  $G_{Lf}$  and  $G_{Rf}$  between the NMSSM and the MSSM.

#### 1. A long-lived slepton

The relic density of dark matter is well described by the coannihilation mechanism [15]. It requires the small mass difference  $\delta m$  between the neutralino LSP and the slepton NLSP. The two-body decay  $\tilde{l} \rightarrow \tilde{\chi}_1^0 + \tau$  is kinematically forbidden when  $\delta m < m_\tau$ . Let us first consider the case where  $c_e = c_\mu = 0$  and  $c_\tau = 1$ . In this case, the flavor is conserved and the slepton is stau. The only allowed decay channel is three- and four-body decay. These decay rates are suppressed due to the small phase space and the small couplings, and hence the sleptons become long-lived. Then it survives until the BBN era to form bound states with nuclei. Such long-lived slepton can account for the discrepancy of the lithium by exotic nuclear reactions with the bound state [6–11] (see also [16]).

This situation radically changes when  $c_e$  and/or  $c_\mu$  are nonzero as the flavor violating two-body decay channels

$$\tilde{l} \rightarrow \tilde{\chi}_1^0 + f, \quad f \ni e, \mu \quad (13)$$

open up. These channels do not suffer from the phase-space suppressions and the coupling suppressions, and thus may make the slepton lifetime much shorter. We note that the lifetime is proportional to  $(G_{Lf} + G_{Rf})^{-2}$  where  $f = \mu$  and  $e$ .

## 2. Exotic BBN reactions

There are three types of exotic BBN reactions with the long-lived slepton.

First one is the internal conversion processes [7, 17],

$$(^7\text{Be } \tilde{l}^-) \rightarrow ^7\text{Li} + \tilde{\chi}_1^0 + \nu_l, \quad (14a)$$

$$(^7\text{Li } \tilde{l}^-) \rightarrow ^7\text{He} + \tilde{\chi}_1^0 + \nu_l, \quad (14b)$$

where,  $(X \tilde{l}^-)$  represents bound state of a nucleus  $X$  and the slepton. Notice that not only  $^7\text{Li}$  but also  $^7\text{Be}$  must be converted since  $^7\text{Be}$  produces  $^7\text{Li}$  by the electron capture in late universe.

The second one is the catalyzed fusion process [18–20],

$$(^4\text{He } \tilde{l}^-) + \text{D} \rightarrow ^6\text{Li} + \tilde{l}^-, \quad (15)$$

where D represents deuteron.

The last one is the  $^4\text{He}$  spallation processes [10]:

$$(^4\text{He } \tilde{l}^-) \rightarrow \tilde{\chi}_1^0 + \nu_l + \text{T} + n, \quad (16a)$$

$$(^4\text{He } \tilde{l}^-) \rightarrow \tilde{\chi}_1^0 + \nu_l + \text{D} + 2n, \quad (16b)$$

$$(^4\text{He } \tilde{l}^-) \rightarrow \tilde{\chi}_1^0 + \nu_l + p + 3n, \quad (16c)$$

where triton (T), deuteron, proton ( $p$ ), and neutron ( $n$ ) are produced from  $^4\text{He}$ .

The timescale to form bound state ( $^7\text{Be } \tilde{l}^-$ ) is  $\mathcal{O}(10^3)$  s [8]. This timescale is important because the primordial  $^7\text{Li}$  exists as beryllium-7 in the BBN era. The internal conversion processes (14) proceed much faster and thus  $^7\text{Be}$  is very efficiently destroyed. We note that  $^7\text{Li}$  from (14a) is also destroyed by background protons. Thus if the slepton lifetime is longer than  $10^3$  s, we can obtain observed abundance of  $^7\text{Li}$  through the internal conversion processes. We can control the timescales of the internal conversion processes (14) by changing free parameters in  $G_{L\tau}$ ,  $G_{R\tau}$ , and  $\delta m$ .

The timescale to form bound state ( $^4\text{He } \tilde{l}^-$ ) is  $\mathcal{O}(10^4)$  s [8]. The abundance of  $^6\text{Li}$  has sever upper bound,  $^6\text{Li}/^7\text{Li} = 0.046 \pm 0.022$  [13]. The abundance through the catalyzed fusion process (15) strongly depends on the slepton lifetime. Therefore, since the process can overproduce  $^6\text{Li}$ , it gives an upper bound of the slepton lifetime. On the other hand, it is argued that tiny primordial abundance of  $^6\text{Li}$  exists. This is called the  $^6\text{Li}$  problem [13]. We can solve this problem by producing tiny amount of  $^6\text{Li}$  through the catalyzed fusion process (15). In the situation, the slepton lifetime has to be tuned so that sufficient amount of  $^6\text{Li}$  is produced. Therefore, the catalyzed fusion process (15) can also give lower bound of the slepton lifetime. The amount of  $^6\text{Li}$  can be controlled by changing free parameters in  $G_{Lf}$  and  $G_{Rf}$  through the slepton lifetime since the timescale of the catalyzed fusion process (15) depends on neither  $G_{Lf}$  nor  $G_{Rf}$  where  $f = \tau, \mu$ , and  $e$ .

The standard BBN can predict observed abundances of  $^3\text{He}$  and D. Therefore, the  $^4\text{He}$  spallation processes (16)

should not be efficient, which gives upper bound on their timescales and the slepton lifetime. We can also control these timescales by changing the parameters in  $G_{L\tau}$ , and  $G_{R\tau}$  so that the overproduction of T ( $^3\text{He}$  in later time) and D does not occur.

## 3. Difference between the NMSSM and the MSSM

In the limit of  $\lambda, \kappa \rightarrow 0$  fixing  $\mu_{\text{eff}}$ , the NMSSM with bino-like LSP is reduced to the MSSM as long as we consider the exotic BBN processes [9–11]. In the singlino-like LSP scenario, the couplings  $G_{Lf}$  and  $G_{Rf}$  are in general smaller than those in the MSSM, and hence the slepton lifetime tends to be much longer than that in the MSSM. The couplings  $G_{L\tau}$  and  $G_{R\tau}$  need to be large so that the timescales of the internal conversion processes (14) are sufficiently short to solve the  $^7\text{Li}$  problem. In such situation, however, the timescales of the  $^4\text{He}$  spallation processes (16) are also short, and thus  $^3\text{He}$  and D can be overproduced. We have to adjust the slepton lifetime to avoid the overproduction taking the flavor mixings of the slepton into account.

Taking these facts into account, we will search for parameter sets which can solve the lithium problems along the strategy that we show in the next section.

## III. STRATEGY

We acquire parameter sets giving observed light element abundances, the Higgs mass, and dark matter relic density according to the following strategy.

### A. Search for candidate region on $\lambda$ - $\kappa$ plane

We narrow the parameter space on  $\lambda$ - $\kappa$  plane requiring that the slepton lifetime,  $\tau_{\tilde{l}}$ , and the timescale of the internal conversion processes,  $\tau_{\text{IC}}$ , are in range where the lithium problems can be solved. Then the parameter region on  $\lambda$ - $\kappa$  plane can be constrained since the lifetime and the timescale depends on the couplings  $G_{Lf}$  and  $G_{Rf}$ . We require the following conditions to be satisfied when  $\delta m$  is around 0.1 GeV which is favored in our scenario [7–11].

The requirement for the slepton lifetime is

$$10^3 \text{ s} < \tau_{\tilde{l}} < 10^5 \text{ s}. \quad (17)$$

As we mentioned in Sec. II C 2, the slepton lifetime must be at least longer than the timescale of bound-state formation for the internal conversion processes (14),  $\mathcal{O}(10^3)$  s, in order to obtain observed  $^7\text{Li}$  abundance. The upper bound  $10^5$  s comes from the requirement that the slepton has sufficient longevity to produce sufficient amount of  $^6\text{Li}$  avoiding the overproduction through the catalyzed fusion process (15).

We require the timescale of the internal conversion processes to be much shorter than the slepton lifetime so that the internal conversion (14) works sufficiently and then solve the  ${}^7\text{Li}$  problem,

$$\tau_{\text{IC}} < 0.1\tau_{\tilde{l}}. \quad (18)$$

Since the parameter dependence on the timescale is different from that of the slepton lifetime, we introduce the requirement Eq. (18) independently from the requirement of the lifetime Eq. (17).

In addition, we require that the fraction of singlino in the neutralino LSP is larger than 90%,

$$N_{1\tilde{S}}^2 > 0.9, \quad (19)$$

for the singlino-like LSP scenario and the fraction of bino in the neutralino LSP is larger than 90%,

$$N_{1\tilde{B}}^2 > 0.9, \quad (20)$$

for the bino-like LSP scenario.

### B. Selection of parameter sets

We impose constraints from the recent results of observational relic density of dark matter and experimental value of the Higgs mass in addition to those in Sec. III A. We use NMSSMTools 4.1.1 [21–25]. to calculate dark matter relic density and the Higgs mass.<sup>1</sup> Then we select several parameter sets from the region we obtained in the previous step.

The latest result for observed abundance of dark matter is reported by the Planck Collaboration

$$0.1118 \leq \Omega_{\text{DM}} h^2 \leq 0.1280 \quad (21)$$

at the  $3\sigma$  level [4], and we apply this result as a constraint. In the calculation, we use MicrOMEGAs [27] included in NMSSMTools.

The latest experimental value of the Higgs mass is

$$m_h = 125.7 \pm 0.3(\text{stat.}) \pm 0.3(\text{syst.}) \text{ GeV} \quad (22)$$

by the CMS Collaboration [28], and

$$m_h = 125.5 \pm 0.2(\text{stat.})_{-0.6}^{+0.5}(\text{syst.}) \text{ GeV} \quad (23)$$

by the ATLAS Collaboration [29], respectively. There are several public codes for calculation of the Higgs mass, and it is known that uncertainty about  $\pm 3$  GeV exists among their calculations [30–34]. Then we take the uncertainty into account in this study and require that

$$m_h = 125.6 \pm 3.0 \text{ GeV}. \quad (24)$$

<sup>1</sup> In the neutralino sector, NMSSMTools includes 1-loop radiative corrections for  $M_1$ ,  $M_2$ , and  $\mu_{\text{eff}}$  when it numerically diagonalize the mass matrix of the neutralino Eq. (6). On the other hand, we do not include the loop contributions in calculations of the neutralino masses and mixings for simplicity since the loop effects are negligible in our discussion.

### C. Constraints from BBN

We perform reaction network calculations for light elements including the exotic nuclear-reactions with the bound-state effects. The baryon to photon ratio is taken to be  $\eta = (6.04 \pm 0.08) \times 10^{-10}$  [4]. Then we obtain allowed regions in the parameter space as a function of  $\delta m$  to fit observational light element abundances.

We adopt following observational bounds on light element abundances: the lithium 7 to hydrogen ratio  $\text{Log}_{10}({}^7\text{Li}/\text{H}) = -9.63 \pm 0.06$  [12], the lithium 6 to lithium 7 ratio  ${}^6\text{Li}/{}^7\text{Li} = 0.046 \pm 0.022$  [13], the deuterium to hydrogen ratio  $\text{D}/\text{H} = (2.80 \pm 0.20) \times 10^{-5}$  [35], and the helium 3 to deuterium ratio  ${}^3\text{He}/\text{D} < 0.87 + 0.27$  [36]. It is notable that our scenario does not change the abundance of  ${}^4\text{He}$  significantly.

For the moment, in order to obtain milder bounds as conservatively as possible we do not adopt newer observational bounds on the abundance of deuterium such as  $\text{D}/\text{H} = (2.54 \pm 0.05) \times 10^{-5}$  and  $\text{D}/\text{H} = (2.53 \pm 0.04) \times 10^{-5}$ . They were quite-recently reported by Pettini and Cooke 2012 [37] and Cooke et al 2013 [38], respectively. About such small errors, we need third-party verifications as soon as possible.

## IV. RESULTS

Now we show the results following the strategy shown in the previous section. The neutralino LSP is either singlino- or bino-like. We have two types of phenomenologically favored parameter spaces in each case: one is the region where  $\lambda$  and  $\kappa$  are relatively small, and  $\tan\beta$  is large; the other is the region where  $\lambda$  and  $\kappa$  are relatively large, and  $\tan\beta$  is small. Therefore, we have four cases. However, we do not consider the case where the neutralino LSP is bino-like,  $\lambda$  and  $\kappa$  are relatively small, and  $\tan\beta$  is large. In the limit of  $\lambda, \kappa \rightarrow 0$  with fixed  $\mu_{\text{eff}}$ , the NMSSM is reduced to the MSSM, so the results are same as that in the MSSM [9–11]. We consider the other three cases in the followings.

First we consider the case where the neutralino LSP is singlino-like,  $\lambda$  and  $\kappa$  are relatively small ( $\kappa \lesssim \lambda \ll 1$ ), and  $\tan\beta$  is large ( $\gtrsim 30$ ) [23]. We take four points of parameter sets and denote them by SS-1, SS-2, SS-3, and SS-4, respectively. Here “SS” stands for the “S”inglino-like neutralino LSP and “S”mall couplings region.

Next we consider the case where the neutralino LSP is singlino-like,  $\lambda$  and  $\kappa$  are relatively large ( $0.5 \lesssim \lambda \lesssim 0.7$  and at most same order value of  $\kappa \lesssim \lambda$ ) and  $\tan\beta$  is small ( $\sim 2$ ). Large  $\lambda$  with small  $\tan\beta$  leads to large tree contributions to the Higgs mass (the second and the third terms in Eq. (4)) while it is small in the region in the first case. Actually,  $\lambda$  has its maximal value  $\sim 0.7$  though it depends on  $\kappa$  (see for example Table 1 in [26]). This comes from the requirement to avoid the Landau pole up to the GUT scale. The value of  $\kappa$  should not be much smaller than  $\lambda$  in order to obtain large tree

contributions to the Higgs mass; in this case the negative contribution (the third term in Eq. (4)) do not become significant. Therefore, we investigate the range from at least 0.5 to 0.7 for  $\lambda$ , and the same order of magnitude but relatively small range of  $\kappa$ . We take  $\tan\beta \sim 2$  since the tree contributions in Eq. (4) are maximized around the value with large  $\lambda$ . We take four points of parameter sets and denote them by SL-1, SL-2, SL-3, and SL-4, respectively. Here ‘‘SL’’ stands for the ‘‘S’’inglino-like neutralino LSP and ‘‘L’’arge couplings region.

In the third case we consider the bino-like neutralino LSP and search the same region on  $\lambda$ - $\kappa$  plane as in the second case [23, 26]. In the NMSSM the tree contributions to the Higgs mass are large, which is different from those in the MSSM where well tuned 1-loop contribution is required. We take four points of parameter sets and denote them by BL-1, BL-2, BL-3, and BL-4, respectively. Here ‘‘BL’’ stands for the ‘‘B’’ino-like neutralino LSP and ‘‘L’’arge couplings region.

In the following results, we fix the parameters as  $m_{\tilde{\chi}_1^0} = 350$  GeV, and  $\sin\theta_f = 0.8$  for  $f = e, \mu$ , and  $\tau$ .

### A. Singlino-like neutralino LSP; small $\lambda$ - $\kappa$ region with large $\tan\beta$

#### 1. Benchmark points

Figure 1 shows the region on  $\lambda$ - $\kappa$  plane with large  $\tan\beta$  where the requirements, Eqs. (17)-(19), are satisfied. The left and right panels show the results for  $c_e = 2 \times 10^{-9}$  and  $10^{-9}$ , respectively. We discuss only the case for  $\tan\beta = 30$  in each panel since we obtain almost same results for  $\tan\beta > 30$ . The mass of the lightest neutralino,  $m_{\tilde{\chi}_1^0} \simeq \mu_\kappa$ , is almost equal to that of the next-to-lightest one,  $m_{\tilde{\chi}_2^0} \simeq \mu_{\text{eff}}$ , on the dotted line. Above the dotted line, the singlino-like neutralino is no longer the lightest one.

We can see that larger  $\lambda$  and smaller  $\kappa$  are allowed by larger  $c_e$  with fixed  $\tan\beta$ . This is explained by the requirement Eq. (17) and the dependence of the couplings, Eqs. (8) and (9), on  $\lambda$  and  $\kappa$ . These couplings become large as  $\kappa$  increase, and/or  $\lambda$  decreases. The slepton lifetime becomes short as the couplings and/or  $c_e$  increase. Therefore, larger  $c_e$  gives shorter slepton lifetime and allows the region with larger  $\lambda$  and smaller  $\kappa$ .

To check which requirements determine the favored region in Fig. 1, we draw Fig. 2 to show the distribution of the quantities which are relevant to the requirements, Eqs. (17)-(19). The parameters used are  $c_e = 2 \times 10^{-9}$ ,  $m_{\tilde{\chi}_1^0} = 350$  GeV,  $\delta m = 0.1$  GeV,  $\sin\theta_f = 0.8$ ,  $\tan\beta = 30$ ,  $M_1 = 500$  GeV, and  $M_2 = 1000$  GeV. From the result we can see the favored region is determined by the requirement for the slepton lifetime of Eq. (17).

We take four reference points in the favored region for  $\tan\beta = 30$  (red region in Fig. 1) as shown in Table I. Table II shows the spectra and observables at these points. We omit small flavor mixing of the slepton in this calculation, and thus SS-1 and SS-2 give same results. All the

dimensionful values are shown in GeV. The top rows show input parameters. We assume the relations for gaugino masses

$$M_1 = M_2/2, M_3 = 3M_2, \quad (25)$$

similar to the GUT relation, and, for simplicity, universal input soft-masses for each squark and slepton,

$$\begin{aligned} m_{\tilde{Q}_{1,2}} &= m_{\tilde{Q}_3} = m_{\tilde{U}_{1,2}} = m_{\tilde{U}_3} = m_{\tilde{D}_{1,2}} = m_{\tilde{D}_3}, \\ m_{\tilde{L}_{1,2}} &= m_{\tilde{L}_3}, \quad m_{\tilde{E}_{1,2}} = m_{\tilde{E}_3}. \end{aligned} \quad (26)$$

The middle rows show output spectra. Every points give the observed Higgs mass Eq.(24). At these points,  $m_h$  receives significant contribution from the 1-loop correction (the fourth term in Eq. (4)) by the maximal mixing and large stop masses because the tree contributions (the second and third terms in Eq. (4)) are small.

In the bottom rows, we show relic density of the lightest neutralino, spin-independent cross section between the lightest neutralino and nucleon, the SUSY contribution to the muon anomalous magnetic moment, and the branching ratios of rare decays  $B_s \rightarrow \mu^+ \mu^-$  and  $b \rightarrow s\gamma$ , from top to bottom. At each point, the dark matter relic density is in range of the measured value [4]. The spin-independent cross section at each point is about four orders of magnitude smaller than the present experimental bound [45]. The latest experimental result for the SUSY contribution to the anomalous magnetic moment is,

$$\delta a_\mu = a_\mu^{\text{exp}} - a_\mu^{\text{SM}} = (26.1 \pm 8.0) \times 10^{-10}, \quad (27)$$

where  $a_\mu \equiv (g-2)_\mu/2$  [39–41]. For the branching ratio of  $B_s \rightarrow \mu^+ \mu^-$ , the CMS Collaboration recently reported in Ref. [42] as

$$\text{BR}(B_s \rightarrow \mu^+ \mu^-) = 3.0_{-0.9}^{+1.0} \times 10^{-9} \quad (28)$$

and also the LHCb Collaboration reported in Ref. [43] as

$$\text{BR}(B_s \rightarrow \mu^+ \mu^-) = 2.9_{-1.0}^{+1.1}(\text{stat.})_{-0.1}^{+0.3}(\text{sys.}) \times 10^{-9}. \quad (29)$$

The branching ratio of  $B \rightarrow X_s \gamma$  [44] is given by

$$\text{BR}(B \rightarrow X_s \gamma) = (3.43 \pm 0.21 \pm 0.07) \times 10^{-4}. \quad (30)$$

At each point,  $\delta a_\mu$  and  $\text{BR}(B_s \rightarrow \mu^+ \mu^-)$  are in the ranges of  $2\sigma$  and  $1\sigma$ . The branching ratio of  $b \rightarrow s\gamma$  is in the  $2\sigma$  range at SS-3 and SS-4.

#### 2. BBN results at the benchmark points

The left panels in Fig. 3 show the slepton lifetime  $\tau_{\tilde{l}}$  (red-solid line; ‘‘slepton lifetime’’), the timescales of the internal conversion processes (14a) (blue-solid line; ‘‘ ${}^7\text{Be} \rightarrow {}^7\text{Li}$ ’’), (14b) (blue-dash-dotted line; ‘‘ ${}^7\text{Li} \rightarrow {}^7\text{He}$ ’’), the  ${}^4\text{He}$  spallation processes (16a) (brown-solid line; ‘‘tn’’), (16b) (brown-dashed line; ‘‘dnn’’), and

(16c) (brown-dash-dotted line; “pnnn”), as a function of the mass difference between the slepton and the neutralino at SS-1, SS-2, SS-3, and SS-4 from top to bottom, respectively. The horizontal black-dashed line represents the timescale of the catalyzed fusion process (15) [19] at the temperature  $T = 5$  keV ( $5 \times 10^4$  s) when ( ${}^4\text{He } \tilde{l}^-$ ) is formed.

We show the allowed regions in the right panels of Fig. 3 which we obtain by comparing theoretical values to observational ones for light element abundances at SS-1, SS-2, SS-3, and SS-4 from top to bottom, respectively. Horizontal axis is the mass difference between the slepton NLSP and the neutralino LSP, and vertical axis is the yield value of the slepton at the beginning of the BBN,  $Y_{\tilde{l}^-} = n_{\tilde{l}^-}/s$ , where  $n_{\tilde{l}^-}$  is the number density of the slepton and  $s$  is the entropy density. The regions surrounded by magenta-dotted(-solid) lines are allowed by observed  ${}^7\text{Li}/\text{H}$  abundance at  $2\sigma(3\sigma)$ . The regions between the blue-solid line and the blue region are allowed by observed  ${}^6\text{Li}/{}^7\text{Li}$  abundance at  $2\sigma$ . The orange-solid lines (“Theoretical”) represent the yield value of the slepton calculated with the parameters in Table. II. The colored regions are excluded for  ${}^6\text{Li}/{}^7\text{Li}$  (blue region; “ ${}^6\text{Li}/{}^7\text{Li}$  excluded”),  ${}^3\text{He}/\text{D}$  (red region; “ ${}^3\text{He}/\text{D}$  excluded”), and  $\text{D}/\text{H}$  (cyan region; “ $\text{D}/\text{H}$  excluded”), respectively. The shaded and dotted regions are allowed by only  ${}^7\text{Li}/\text{H}$  ( $3\sigma$ ) and both  ${}^7\text{Li}/\text{H}$  ( $3\sigma$ ) and  ${}^6\text{Li}/{}^7\text{Li}$  ( $2\sigma$ ), respectively, since  $Y_{\tilde{l}^-}$  can be reduced by changing  $c_\mu$  and  $\theta_f$ . At each point, we obtain allowed region from  ${}^7\text{Li}/\text{H}$  ( $3\sigma$ ) and  ${}^6\text{Li}/{}^7\text{Li}$  ( $2\sigma$ ) simultaneously.

We see in the right panels of Fig. 3 that the allowed region from  ${}^7\text{Li}/\text{H}$  on the curve of the slepton yield value is in the range of  $\delta m \sim (0.04, 0.07)$ ,  $(0.07, 0.1)$ ,  $(0.07, 0.1)$ , and  $0.1$  GeV at the points SS-1, SS-2, SS-3, and SS-4 respectively. We note that the catalyzed fusion process affects the abundance of the  ${}^6\text{Li}$  in these allowed regions even if the timescale of the reaction is much longer than the slepton lifetime and the timescales of the  ${}^4\text{He}$  spallation processes. This is because the yield value of the slepton is much larger than observed abundance of the  ${}^6\text{Li}$ . We roughly calculate a yield value of the  ${}^6\text{Li}$  through the catalyzed fusion as follows;

$$\Delta Y_{6\text{Li}} = Y_{\tilde{l}^-} e^{-\tau_{\text{B.F.}}/\tau_{\tilde{l}^-}} \frac{\Gamma_{\text{C.F.}}}{\Gamma_{\text{Sp.}} + \Gamma_{\tilde{l}^-} + \Gamma_{\text{C.F.}}}, \quad (31)$$

where  $\Delta Y_{6\text{Li}}$  is the yield value of the  ${}^6\text{Li}$ ,  $\tau_{\text{B.F.}}$  is a timescale of ( ${}^4\text{He } \tilde{l}^-$ ) formation,  $\Gamma_{\tilde{l}^-}$  is a decay rate of the slepton,  $\Gamma_{\text{Sp.}}$  and  $\Gamma_{\text{C.F.}}$  are a reaction rate of the  ${}^4\text{He}$  spallation processes and the catalyzed fusion process, respectively. In Eq (31),  $Y_{\tilde{l}^-} e^{-\tau_{\text{B.F.}}/\tau_{\tilde{l}^-}}$  represents a yield value of the bound state, and the factor at the last of the right hand side is the branching ratio of the bound state to the catalyzed fusion reaction. Here we consider the predicted value of the  ${}^6\text{Li}$  along with the slepton yield value which we calculate with the parameters shown in Table II. We put the constraint from the observed value

on the calculated value as follows;

$$\frac{Y_{6\text{Li,Ob.}}}{Y_{\tilde{l}^-}} \simeq 10^{-8} \gtrsim e^{-\tau_{\text{B.F.}}/\tau_{\tilde{l}^-}} \frac{\Gamma_{\text{C.F.}}}{\Gamma_{\text{Sp.}} + \Gamma_{\tilde{l}^-} + \Gamma_{\text{C.F.}}}, \quad (32)$$

where we choose the yield value as  $Y_{\tilde{l}^-} \simeq 10^{-13}$  and  $Y_{6\text{Li,Ob.}} \simeq \mathcal{O}(10^{-21})$  which is the observed yield value of  ${}^6\text{Li}$  [13]. We take the timescale of the bound state formation  $\tau_{\text{B.F.}} \simeq 5 \times 10^4$  s (see the Fig. 1 of Ref. [8]), and  $\Gamma_{\text{C.F.}} \simeq \mathcal{O}(10^{-10})$  s $^{-1}$ . We see that  $\tau_{\tilde{l}^-} \simeq 10^4$  s and  $\Gamma_{\text{Sp.}} \simeq 10^{-5}$  s $^{-1}$  in the allowed region at the left panels of Fig. 3. We confirm that the calculated yield value of  ${}^6\text{Li}$  is consistent with that of the observational value at the allowed region.

We also see that the allowed range of the mass difference is different in each point. This difference can be explained as follows. The selectron mixing is smaller at SS-2 than at SS-1. The smaller mixing results in smaller coupling  $G_{L,Re}$  and hence longer slepton lifetimes than that at SS-1 shown in the left panels in Fig. 3. The longer the lifetime is, the more the exotic BBN reactions occur because a larger number of the sleptons remains until they form bound state with  ${}^7\text{Be}$ . More  ${}^7\text{Be}$  are destroyed by the internal conversion processes at SS-2 than at SS-1. In such a situation, the yield value of the slepton required by observed  ${}^7\text{Li}$  abundance can be smaller for the same  $\delta m$ . In fact, comparing the right panels of Fig. 3 of SS-1 and SS-2, we see that the 2 and 3  $\sigma$  lines of  ${}^7\text{Li}/\text{H}$  allows lower yield values and larger  $\delta m$  at SS-2. This result also can be understood in terms of the slepton lifetime. The lifetime must be adjusted to a certain range to solve the Li problems. As mentioned in Sec. II C 1, the lifetime is determined by both  $G_{L,Re}$  and  $\delta m$ . For a fixed lifetime that can explain the observed  ${}^7\text{Li}$  abundance,  $\delta m$  is larger when  $G_{L,Re}$  is smaller. As a result, the allowed region extends to larger  $\delta m$  at SS-2 than at SS-1. For a longer slepton lifetime, on the other hand, more  ${}^3\text{He}$  and D are produced by the  ${}^4\text{He}$  spallation processes, and more  ${}^6\text{Li}$  is produced by the catalyzed fusion process. Thus, the excluded regions due to the  ${}^4\text{He}$  spallation processes (red and cyan regions) and the catalyzed fusion process (blue region) are large compared to those at SS-1.

At the point SS-3,  $\lambda$  is taken slightly larger than the one at SS-1 while  $c_e$  and  $\kappa$  are taken the same. We see that the allowed region is in the range of  $\delta m \sim (0.07, 0.1)$  GeV and is larger than that at SS-1. It is because the lifetime is longer than that at SS-1. However, the reason to make the lifetime longer is different from the case of SS-2. At SS-3, larger  $\lambda$  gives longer slepton lifetime (see top-left panel of Fig. 1), because  $G_{L,Re}$  become smaller than those at SS-1 as shown in Table II, due to the small mixing weights  $N_1$ 's in the lightest neutralino. In Eq. (11), the mixing weights are inversely proportional to  $\mu_\kappa^2 - \mu_{\text{eff}}^2$ . In the singlino-like LSP case,  $\mu_\kappa$  and  $\mu_{\text{eff}}$ , hence  $\kappa$  and  $\lambda$ , must be tuned so that  $G_{L,R}$  are enough large. In fact,  $\kappa$  and  $\lambda$  are tuned well at SS-1. Taking  $\lambda$  larger than that at SS-1 even by a few %,  $G_{L,Re}$  become smaller and hence the lifetime becomes longer. At the same time,  $G_{L,R\tau}$  become smaller. It is still enough large to reduce

${}^7\text{Be}$  by the internal conversion processes but is small for the  ${}^4\text{He}$  spallation processes. Thus, the excluded regions by  ${}^3\text{He}$  and D are narrower than those at SS-2.

At SS-4,  $\kappa$  is taken smaller by 1 % than the one at SS-1 while the other parameters are taken the same. Again, due to the smaller  $\kappa$ , the lifetime of the slepton is longer than at SS-1, and indeed is the longest among the four parameters (see the left panels in Fig. 3). Then  ${}^3\text{He}$  and D are too much produced even for smaller slepton yield values so that the excluded region due to D/H narrows the allowed region. Furthermore, the timescales of the internal conversion processes (14) are longer than those at the other points. Thus more slepton yield value is necessary to obtain the observed abundance of  ${}^7\text{Li}$ , and hence the allowed region at SS-4 is narrower.

In the end, it is important to notice that in the singlino-like LSP case,  $\kappa$  and  $\lambda$  must be well tuned to obtain fast internal conversion processes. As we have shown, only a few % of difference in the parameters drastically change the results. Our scenario is thus very predictable this tuning.

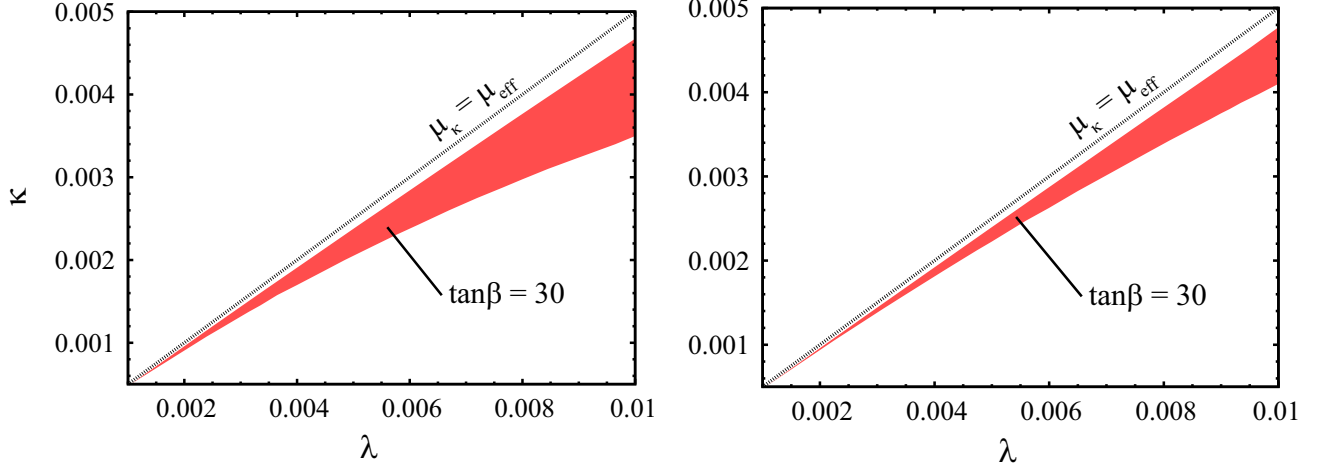


FIG. 1: Favored region (red region; “ $\tan\beta = 30$ ”) in terms of requirements Eqs. (17)-(19) in  $\lambda$ - $\kappa$  plane. Parameters are taken as  $\tan\beta = 30$  and  $c_e = 2 \times 10^{-9}$ (left panel) and  $c_e = 10^{-9}$ (right panel). Other parameters are fixed as  $m_{\tilde{\chi}_1^0} = 350$  GeV,  $\delta m = 0.1$  GeV,  $\sin\theta_f = 0.8$ ,  $M_1 = 500$  GeV, and  $M_2 = 1000$  GeV. The singlino-like neutralino is no longer the lightest one above the dotted line.

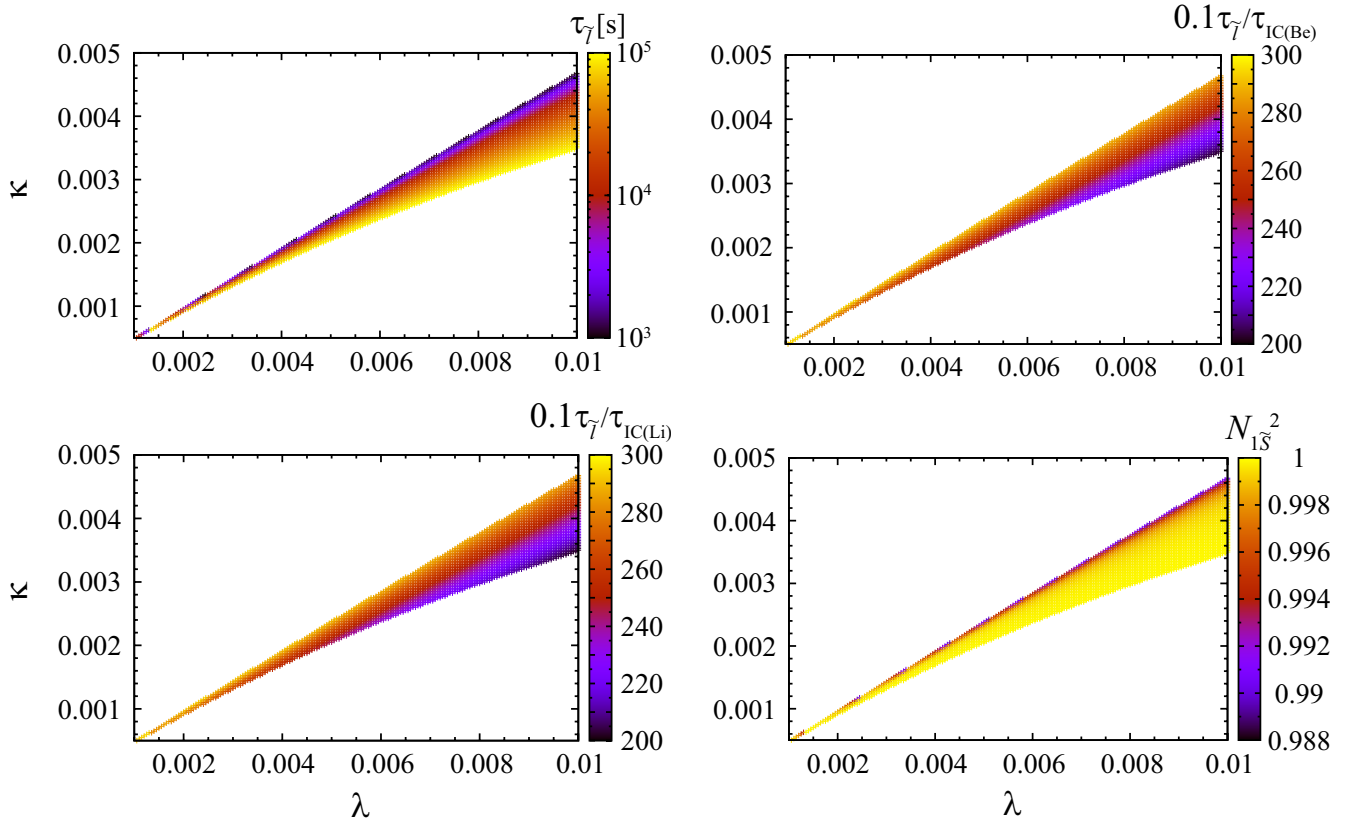


FIG. 2: The distribution of the quantities relevant to the requirements, Eqs. (17)-(19), in the favored region from  $c_e = 2 \times 10^{-9}$  and  $\tan\beta = 30$ . The color bar in each panel shows  $\tau_{\tilde{\gamma}}$  (top-left),  $0.1\tau_{\tilde{\gamma}}/\tau_{IC}$  for  $({}^7\text{Be } \tilde{l}^-) \rightarrow {}^7\text{Li} + \tilde{\chi}_1^0 + \nu_l$  (top-right),  $0.1\tau_{\tilde{\gamma}}/\tau_{IC}$  for  $({}^7\text{Li } \tilde{l}^-) \rightarrow {}^7\text{He} + \tilde{\chi}_1^0 + \nu_l$  (bottom-left), and  $N_{1S}^2$  (bottom-right).

TABLE I: Benchmark points in the favored region of Fig. 1.

Parameters	SS-1	SS-2	SS-3	SS-4
$c_e$	$2 \times 10^{-9}$	$10^{-9}$	$2 \times 10^{-9}$	$2 \times 10^{-9}$
$\lambda$	0.0042	0.0042	0.00425	0.0042
$\kappa$	0.002	0.002	0.002	0.00195

TABLE II: Spectra and observables at each point (see Tab. I). All the dimensionful values are shown in GeV. The top rows show input parameters. SS-1 and SS-2 give common results since we omit small flavor mixing of the slepton. The middle rows show output spectra. The bottom rows show relic density of the lightest neutralino, spin-independent cross section between the lightest neutralino and nucleon, the SUSY contribution to the muon anomalous magnetic moment, and the branching ratios of rare decays  $B_s \rightarrow \mu^+ \mu^-$  and  $b \rightarrow s\gamma$ , and couplings Eqs. (8) and (9) from top to bottom.

Input	SS-1, SS-2	SS-3	SS-4
$M_2$	1000.0	1000.0	1000.0
$A_t$	-3000.0	-4800.0	-7500.0
$m_{\tilde{L}_3}$	391.30	397.06	405.43
$m_{\tilde{E}_3}$	372.99	376.34	381.29
$m_{\tilde{Q}_3}$	1500.0	2000.0	3000.0
$\lambda$	0.0042	0.00425	0.0042
$\kappa$	0.0020	0.0020	0.00195
$A_\lambda$	1000.0	1300.0	1000.00
$A_\kappa$	-100.00	-100.00	-100.00
$\mu_{\text{eff}}$	359.82	363.07	366.76
$\tan \beta$	30.000	30.000	30.000
Output			
$h_1^0$	123.89	126.16	127.30
$h_2^0$	316.70	317.05	314.58
$h_3^0$	3513.4	3939.4	3499.3
$a_1^0$	226.72	226.40	226.02
$a_2^0$	3513.4	3939.4	3499.3
$H^\pm$	3514.2	3940.1	3500.0
$\tilde{t}_1$	1367.9	1897.7	2925.2
$\tilde{t}_2$	1650.6	2235.9	3271.5
$\tilde{\tau}_1$	350.10	350.10	350.10
$\tilde{\tau}_2$	416.67	425.01	437.11
$\tilde{\chi}_1^0$	350.00	350.00	350.00
$\tilde{\chi}_2^0$	355.27	359.35	364.03
$\tilde{\chi}_3^0$	370.74	375.08	380.10
$\tilde{\chi}_4^0$	498.84	498.04	496.76
$\tilde{\chi}_5^0$	1021.1	1027.8	1035.7
$\Omega_{\tilde{\chi}_1^0} h^2$	0.11236	0.12656	0.12490
$\sigma_{\text{SI}} [\text{cm}^2]$	$9.4085 \times 10^{-49}$	$1.4012 \times 10^{-49}$	$3.8721 \times 10^{-50}$
$\delta a_\mu$	$1.1967 \times 10^{-9} (2\sigma)$	$1.2656 \times 10^{-9} (2\sigma)$	$1.2347 \times 10^{-9} (2\sigma)$
$\text{Br}(B_s^0 \rightarrow \mu^+ \mu^-)$	$3.3924 \times 10^{-9} (1\sigma)$	$3.4349 \times 10^{-9} (1\sigma)$	$3.4442 \times 10^{-9} (1\sigma)$
$\text{Br}(b \rightarrow s\gamma)$	$2.5984 \times 10^{-4} (> 3\sigma)$	$2.8109 \times 10^{-4} (2\sigma)$	$3.0311 \times 10^{-4} (2\sigma)$
$G_{L\tau}/c_\tau$	-0.014882	-0.0084607	-0.0055185
$G_{R\tau}/c_\tau$	0.019332	0.011050	0.0072524
$G_{Le}/c_e$	0.00066840	0.00038490	0.00025476
$G_{Re}/c_e$	0.0076689	0.0044158	0.0029225

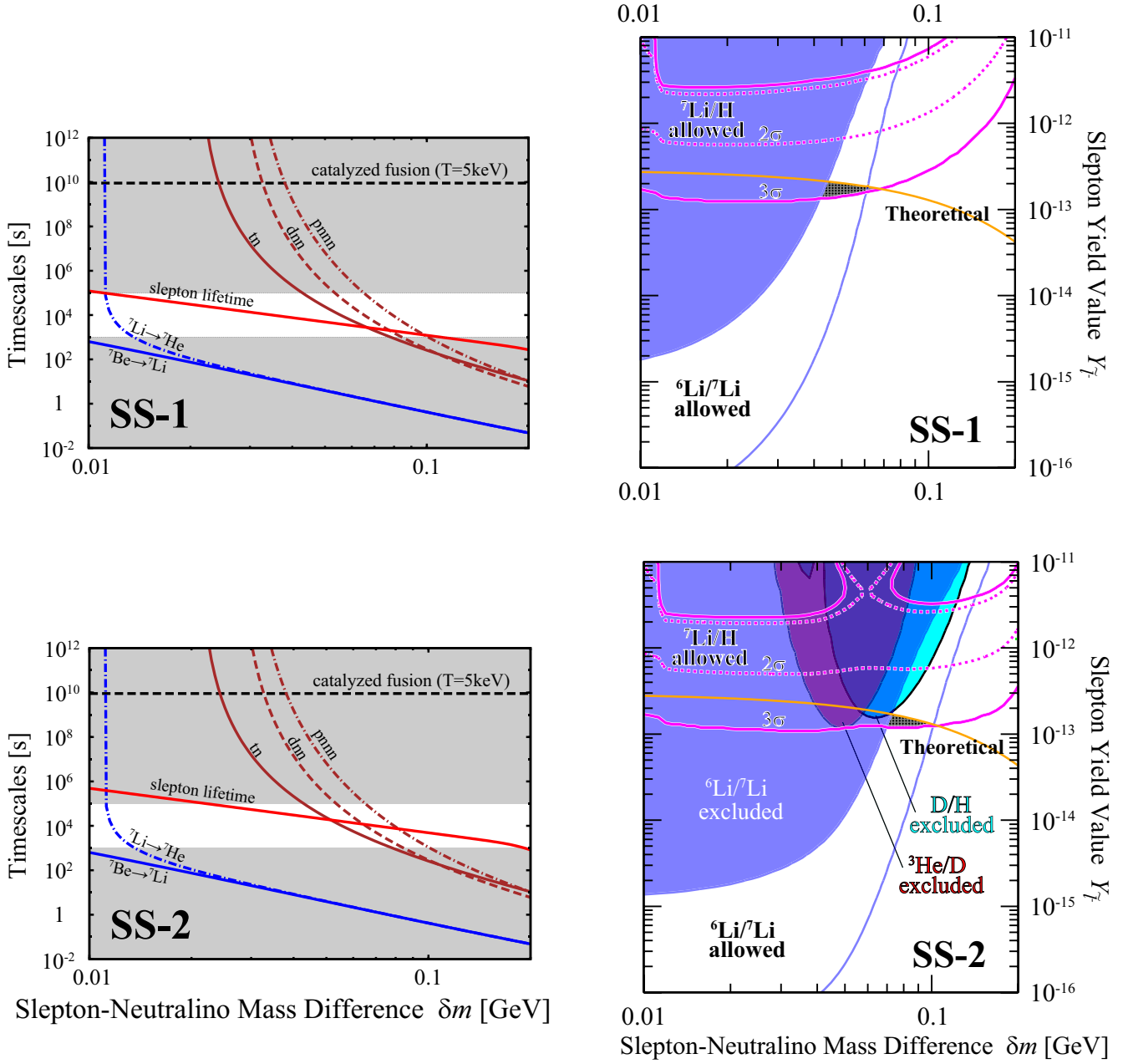


FIG. 3: The left panels show the slepton lifetime  $\tau_{\tilde{\tau}_1}$  (red-solid line; “slepton lifetime”), the timescales of the internal conversion processes (14a) (blue-solid line; “ ${}^7\text{Be} \rightarrow {}^7\text{Li}$ ”), (14b) (blue-dash-dotted line; “ ${}^7\text{Li} \rightarrow {}^7\text{He}$ ”), the  ${}^4\text{He}$  spallation processes (16a) (brown-solid line; “tn”), (16b) (brown-dashed line; “dnn”), and (16c) (brown-dash-dotted line; “pnnn”), as a function of the mass difference between the slepton and the neutralino at SS-1 (top panel) and SS-2 (bottom panel). We also show the timescale of the catalyzed fusion (15) at the temperature  $T = 5$  keV ( $5 \times 10^4$  s) when ( ${}^4\text{He} \tilde{l}^-$ ) is formed as horizontal black-dashed line. In shaded regions Eq. (17) is not satisfied. The right panels show the allowed regions from observational light element abundances on  $\delta m$ - $Y_{\tilde{\tau}_1}$  plane at SS-1 (top panel) and SS-2 (bottom panel). The regions surrounded by magenta-dotted(-solid) lines are allowed by observed  ${}^7\text{Li}/\text{H}$  abundance at  $2\sigma$  ( $3\sigma$ ). The regions between the blue-solid line and the blue region are allowed by observed  ${}^6\text{Li}/{}^7\text{Li}$  abundance at  $2\sigma$  ( $3\sigma$ ). The orange-solid lines (“Theoretical”) represent the yield value of the slepton at the beginning of the BBN as a function of the mass difference. The colored regions are excluded for  ${}^6\text{Li}/{}^7\text{Li}$  (blue region; “ ${}^6\text{Li}/{}^7\text{Li}$  excluded”),  ${}^3\text{He}/\text{D}$  (red region; “ ${}^3\text{He}/\text{D}$  excluded”), and D/H (cyan region; “D/H excluded”), respectively. The shaded and dotted regions are allowed by only  ${}^7\text{Li}/\text{H}$  ( $3\sigma$ ) and both  ${}^7\text{Li}/\text{H}$  ( $3\sigma$ ) and  ${}^6\text{Li}/{}^7\text{Li}$  ( $2\sigma$ ), respectively.

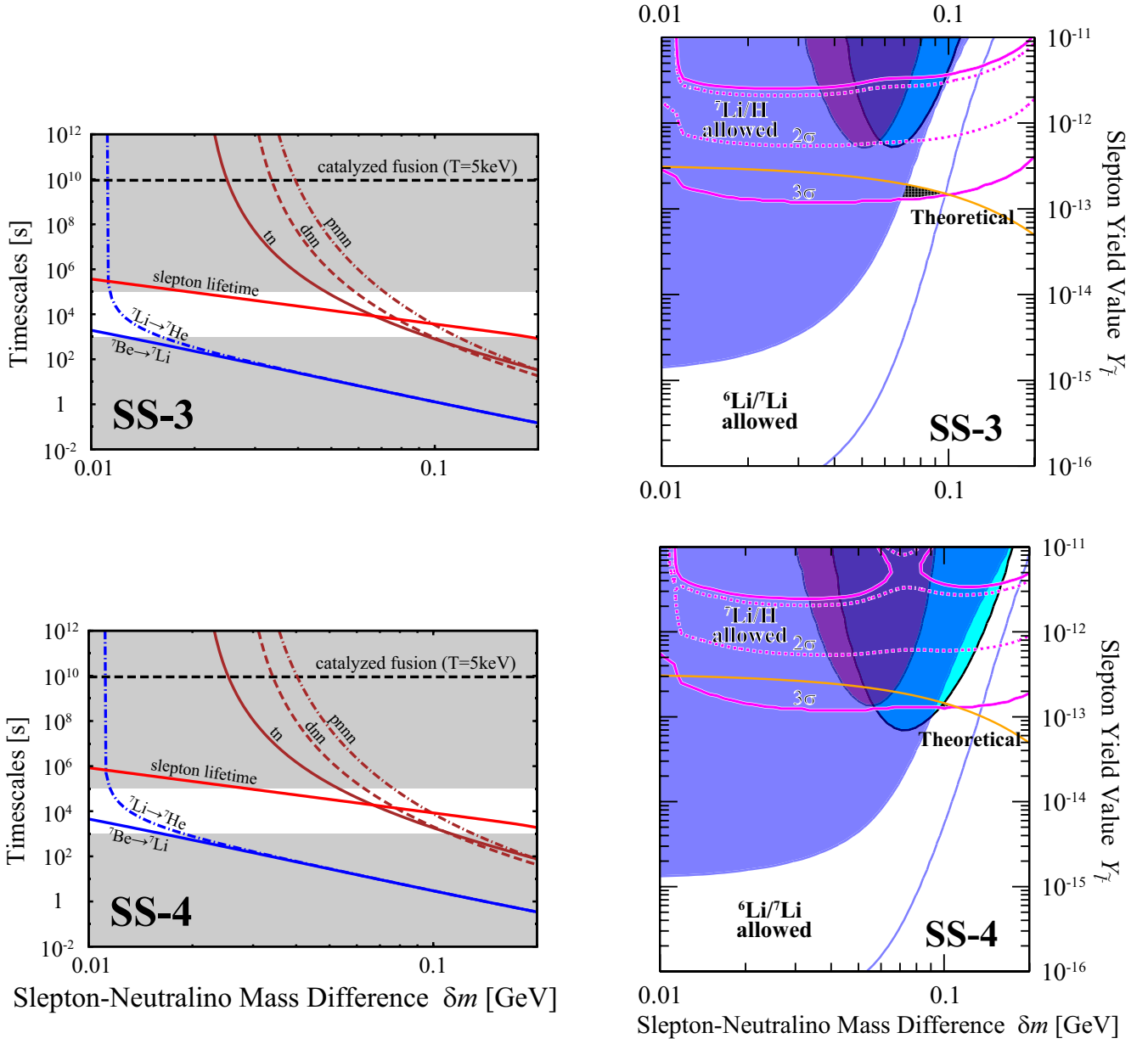


FIG. 3: The results at SS-3 (top panels) and SS-4 (bottom panels) are shown. The lines and regions stand for the same meanings as those in the previous page.

## B. Singlino-like neutralino LSP; large $\lambda$ - $\kappa$ region with small $\tan\beta$

### 1. Benchmark points

Figure 4 shows the favored region on  $\lambda$ - $\kappa$  plane with small  $\tan\beta$  where the requirements, Eqs. (17)-(19), are satisfied. The left and right panels show the results for  $c_e = 5 \times 10^{-10}$  and  $2 \times 10^{-10}$ , respectively. The red and hatched regions are allowed by  $\tan\beta = 2$  and 2.5, respectively.

To check which requirements determine the favored region in Fig. 4, we draw Fig. 5 to show the distribution of the quantities which are relevant to Eqs. (17)-(19). The parameters are  $c_e = 5 \times 10^{-10}$ ,  $m_{\tilde{\chi}_1^0} = 350$  GeV,  $\delta m = 0.1$  GeV,  $\sin\theta_f = 0.8$ ,  $\tan\beta = 2$ ,  $M_1 = 500$  GeV, and  $M_2 = 1000$  GeV. From the result we see the favored region is determined by the requirement for the slepton lifetime Eq. (17).

We take four reference points in the favored region for  $\tan\beta = 2$  (red regions in Fig. 4) as shown in Table III. Table IV shows the spectra and observables at these points. We omit small flavor mixing of the slepton in the calculation, and show the dimensionful values in GeV. Every points give the observed Higgs mass. In this case where  $\lambda$  and  $\kappa$  are large and  $\tan\beta$  is small, the tree contributions in Eq. (4) (the second and the third terms) are significant, and 1-loop contribution (the fourth term) is not so large.

In the bottom rows, we show relic density of the lightest neutralino, spin-independent cross section between the lightest neutralino and nucleon, the SUSY contribution to the muon anomalous magnetic moment, and the branching ratios of rare decays  $B_s \rightarrow \mu^+\mu^-$  and  $b \rightarrow s\gamma$ , from top to bottom. At each point, the dark matter relic density is in range of the measured value [4]. The spin-independent cross section at each point is much larger than those at the points in the previous section and just below the present experimental bound. The calculated values of  $\delta a_\mu$  at the points are out of  $3\sigma$  range, since  $\tan\beta$  is relatively small in this case. For the branching ratio of  $B_s \rightarrow \mu^+\mu^-$  and  $b \rightarrow s\gamma$ , we obtained the values within  $1\sigma$  and  $2\sigma$ , respectively.

### 2. BBN results at the benchmark points

The left panels in Fig. 6 show the slepton lifetime  $\tau_{\tilde{l}}$  (red-solid line; “slepton lifetime”), the timescales of the internal conversion processes (14a) (blue-solid line; “ ${}^7\text{Be} \rightarrow {}^7\text{Li}$ ”), (14b) (blue-dash-dotted line; “ ${}^7\text{Li} \rightarrow {}^7\text{He}$ ”), the  ${}^4\text{He}$  spallation processes (16a) (brown-solid line; “tn”), (16b) (brown-dashed line; “dnn”), and (16c) (brown-dash-dotted line; “pnnn”), as a function of the mass difference between the slepton and the neutralino at SL-1, SL-2, SL-3, and SL-4 from top to bottom, respectively. The horizontal black-dashed line represents the timescale of the catalyzed fusion process (15) [19] at

the temperature  $T = 5$  keV ( $5 \times 10^4$  s) when ( ${}^4\text{He} \tilde{l}^-$ ) is formed. In the right panels horizontal axis is the mass difference between the slepton NLSP and the neutralino LSP, and vertical axis is the yield value of the slepton at the beginning of the BBN.

We show the allowed regions in the right panels of Fig. 6 which we obtain by comparing theoretical values to observational ones for light element abundances at SL-1, SL-2, SL-3, and SL-4 from top to bottom, respectively. The lines and regions are the same as in Fig. 3. Accordingly we obtain allowed region from  ${}^7\text{Li}/\text{H}$  ( $3\sigma$ ) and  ${}^6\text{Li}/{}^7\text{Li}$  ( $2\sigma$ ) simultaneously at each point.

We can get large  $G_{L,R}$  without tuning at the SL points in contrast to SS case, since  $\lambda$  and  $\kappa$  are large enough. Therefore, the couplings  $G_{L,R}$  are almost same as each other at the points SL-3 and SL-4 though  $\lambda$  is larger at SL-3 and  $\kappa$  is smaller at SL-4 than those at SL-1, respectively. Furthermore  $c_e$  is same at each point and the slepton lifetime is almost same. Thus we get similar result at these points.

On the contrary, at SL-2 the selectron mixing is small compared with that of SL-1, and hence the slepton lifetime is longer than the other points. This result in more spallation processes and make the allowed region narrower.

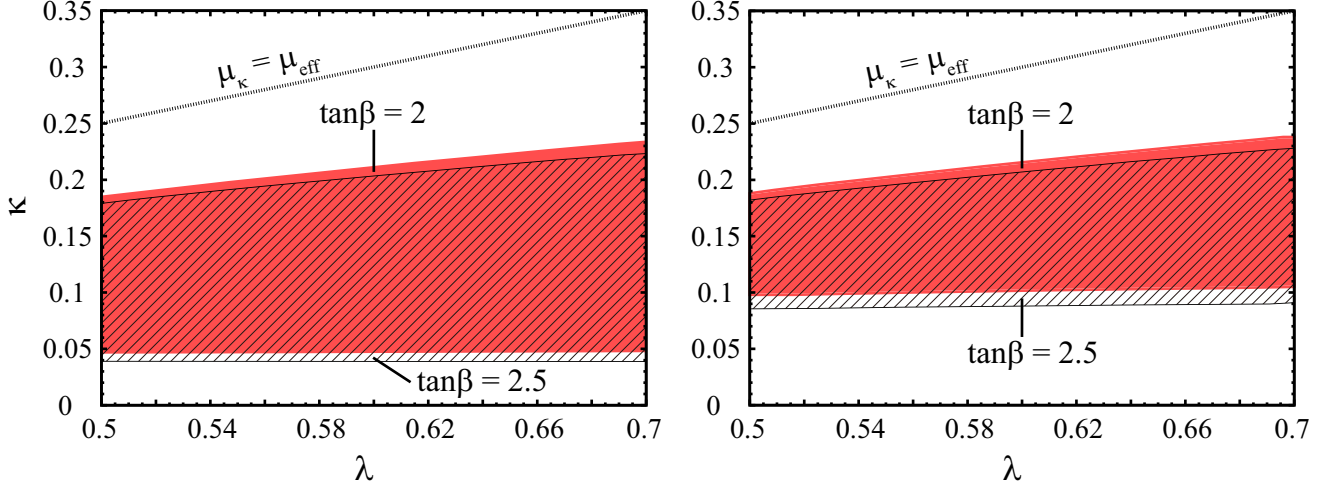


FIG. 4: Favored region in terms of requirements Eqs. (17)-(19) in  $\lambda$ - $\kappa$  plane. We took  $\tan\beta = 2$  and  $2.5$  and  $c_e = 5 \times 10^{-10}$  in left panel ( $c_e = 2 \times 10^{-10}$  in right panel). Fixed parameters are  $m_{\tilde{\chi}_1^0} = 350$  GeV,  $\delta m = 0.1$  GeV,  $\sin\theta_f = 0.8$ ,  $M_1 = 500$  GeV, and  $M_2 = 1000$  GeV. Red and shaded regions are the favored region from  $\tan\beta = 2$  and  $2.5$ , respectively. The singlino-like neutralino is no longer the lightest one above the dotted line.

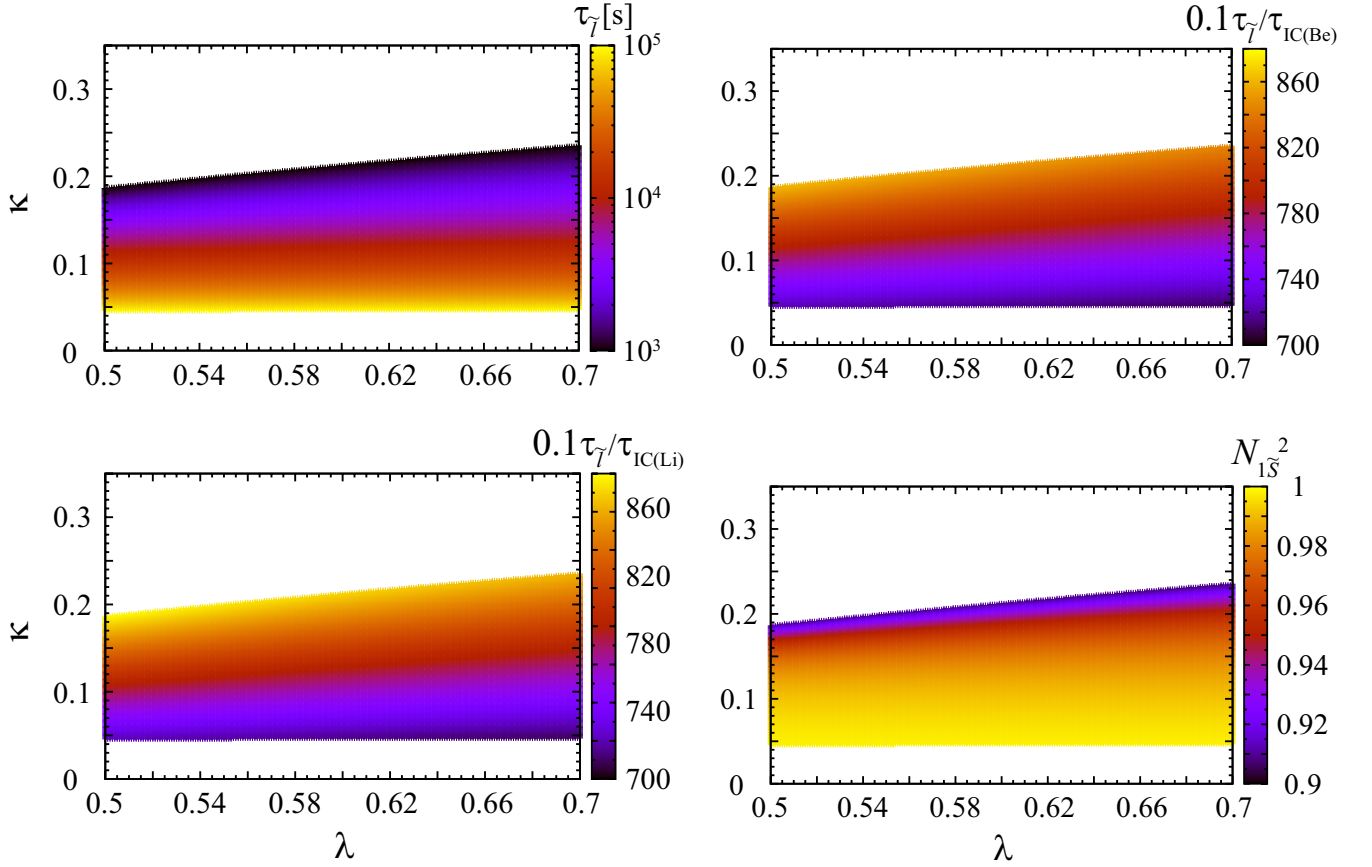


FIG. 5: The distribution of the quantities relevant to the requirements, Eqs. (17)-(19), in the favored region from  $c_e = 5 \times 10^{-10}$  and  $\tan\beta = 2$ . The color bar in each panel shows  $\tau_{\tilde{\gamma}}$  (top-left),  $0.1\tau_{\tilde{\gamma}}/\tau_{IC}$  for  $({}^7\text{Be } \tilde{l}^-) \rightarrow {}^7\text{Li} + \tilde{\chi}_1^0 + \nu_l$  (top-right),  $0.1\tau_{\tilde{\gamma}}/\tau_{IC}$  for  $({}^7\text{Li } \tilde{l}^-) \rightarrow {}^7\text{He} + \tilde{\chi}_1^0 + \nu_l$  (bottom-left), and  $N_{1S}^2$  (bottom-right).

TABLE III: Benchmark points in the favored region of Fig. 4 for  $\tan \beta = 2$ .

Parameters	SL-1	SL-2	SL-3	SL-4
$c_e$	$5 \times 10^{-10}$	$2 \times 10^{-10}$	$5 \times 10^{-10}$	$5 \times 10^{-10}$
$\lambda$	0.68	0.68	0.695	0.68
$\kappa$	0.22	0.22	0.22	0.215

TABLE IV: Spectra and observables at each point (see Tab. III). All the dimensionful values are shown in GeV. The top rows show input parameters. SL-1 and SL-2 give common results since we omit small flavor mixing of the slepton. The middle rows show output spectra. The bottom rows show relic density of the lightest neutralino, spin-independent cross section between the lightest neutralino and nucleon, the SUSY contribution to the muon anomalous magnetic moment, and the branching ratios of rare decays  $B_s \rightarrow \mu^+ \mu^-$  and  $b \rightarrow s\gamma$ , and couplings Eqs. (8) and (9) from top to bottom.

Input	SL-1, SL-2	SL-3	SL-4
$M_2$	1000.0	1000.0	1000.0
$A_t$	-1500.0	-1800.0	-2800.0
$m_{\tilde{L}_3}$	356.86	357.93	361.23
$m_{\tilde{E}_3}$	353.36	353.96	355.84
$m_{\tilde{Q}_3}$	1000.0	1000.0	1000.0
$\lambda$	0.6800	0.6950	0.6800
$\kappa$	0.2200	0.2200	0.2150
$A_\lambda$	1120.0	1180.0	1100.0
$A_\kappa$	-10.000	-10.000	-10.000
$\mu_{\text{eff}}$	527.17	537.90	538.91
$\tan \beta$	2.0000	2.0000	2.0000
Output			
$h_1^0$	127.13	126.66	124.36
$h_2^0$	370.96	354.77	369.96
$h_3^0$	1303.6	1348.4	1313.9
$a_1^0$	152.72	262.92	150.73
$a_2^0$	1303.8	1348.8	1313.8
$H^\pm$	1295.0	1339.0	1304.3
$\tilde{t}_1$	696.15	660.83	528.37
$\tilde{t}_2$	959.18	983.66	1059.9
$\tilde{\tau}_1$	350.10	350.10	350.10
$\tilde{\tau}_2$	363.35	364.99	370.03
$\tilde{\chi}_1^0$	350.00	350.00	350.00
$\tilde{\chi}_2^0$	468.58	471.30	471.37
$\tilde{\chi}_3^0$	547.60	558.78	559.13
$\tilde{\chi}_4^0$	553.96	561.55	562.02
$\tilde{\chi}_5^0$	1013.7	1014.1	1014.1
$\Omega_{\tilde{\chi}_1^0} h^2$	0.12684	0.12672	0.12489
$\sigma_{\text{SI}} [\text{cm}^2]$	$1.8983 \times 10^{-45}$	$3.1914 \times 10^{-45}$	$1.7546 \times 10^{-45}$
$\delta a_\mu$	$1.0707 \times 10^{-10} (> 3\sigma)$	$1.1346 \times 10^{-10} (> 3\sigma)$	$1.3675 \times 10^{-10} (> 3\sigma)$
$\text{Br}(B_s^0 \rightarrow \mu^+ \mu^-)$	$3.5373 \times 10^{-9} (1\sigma)$	$3.5374 \times 10^{-9} (1\sigma)$	$3.5365 \times 10^{-9} (1\sigma)$
$\text{Br}(b \rightarrow s\gamma)$	$3.2030 \times 10^{-4} (2\sigma)$	$3.1658 \times 10^{-4} (2\sigma)$	$3.0507 \times 10^{-4} (2\sigma)$
$G_{L\tau}/c_\tau$	0.0012549	0.0013068	0.0012826
$G_{R\tau}/c_\tau$	0.030877	0.029833	0.029090
$G_{Le}/c_e$	0.0026200	0.0025373	0.0024746
$G_{Re}/c_e$	0.029853	0.028910	0.028196

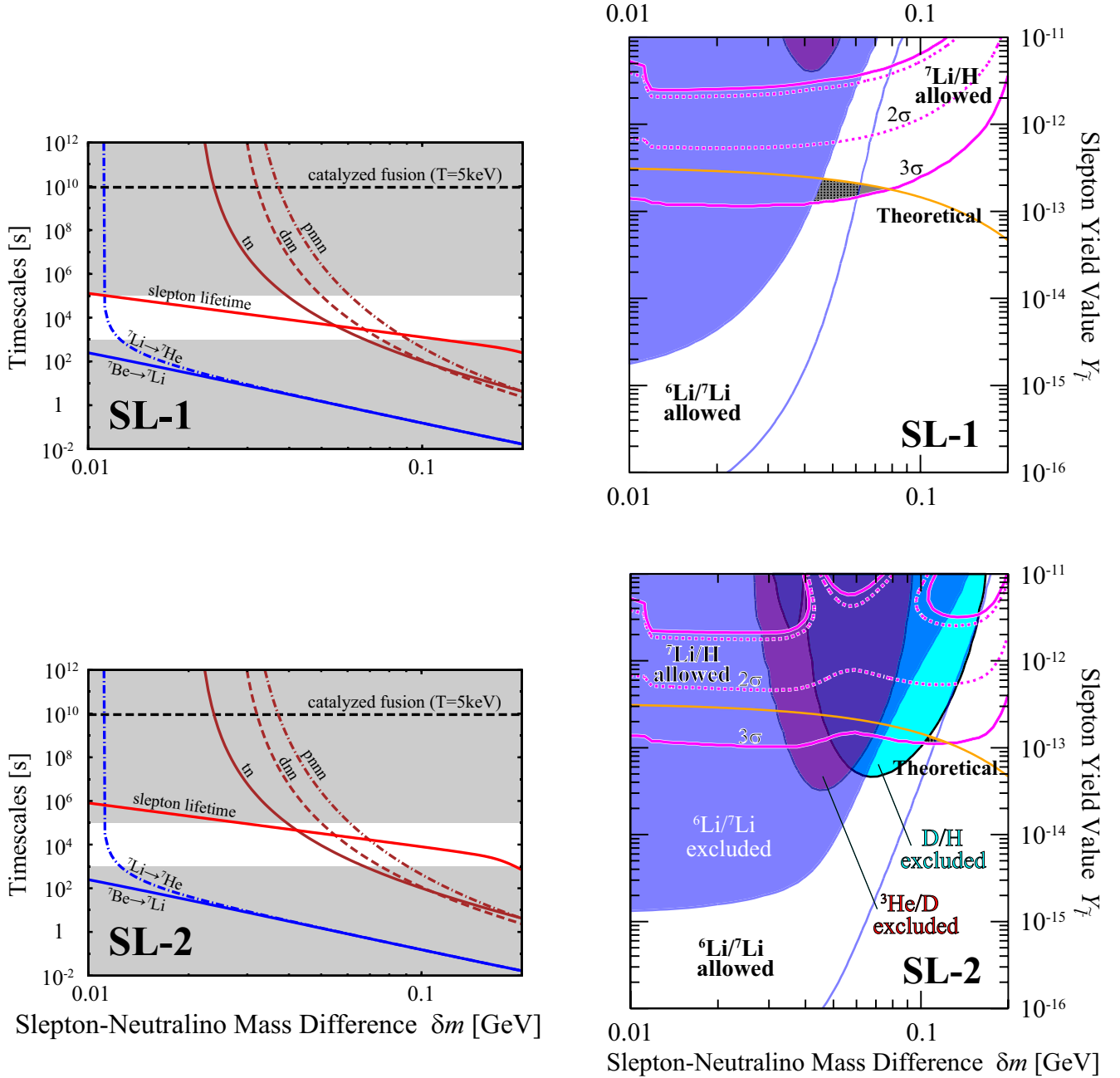


FIG. 6: The left panels show the slepton lifetime  $\tau_{\tilde{\tau}}$  (red-solid line; “slepton lifetime”), the timescales of the internal conversion processes (14a) (blue-solid line; “ ${}^7\text{Be} \rightarrow {}^7\text{Li}$ ”), (14b) (blue-dash-dotted line; “ ${}^7\text{Li} \rightarrow {}^7\text{He}$ ”), the  ${}^4\text{He}$  spallation processes (16a) (brown-solid line; “tn”), (16b) (brown-dashed line; “dnn”), and (16c) (brown-dash-dotted line; “pnnn”), as a function of the mass difference between the slepton and the neutralino at SL-1 (top panel) and SL-2 (bottom panel). We also show the timescale of the catalyzed fusion (15) at the temperature  $T = 5 \text{ keV}$  ( $5 \times 10^4 \text{ s}$ ) when ( ${}^4\text{He } \tilde{l}^-$ ) is formed as horizontal black-dashed line. In the shaded regions, Eq. (17) is not satisfied. The right panels show the allowed regions for observational light element abundances on  $\delta m - Y_{\tilde{\tau}}$  plane at SL-1 (top panel) and SL-2 (bottom panel). The regions surrounded by magenta-dotted(-solid) lines are allowed by observed  ${}^7\text{Li}/\text{H}$  abundance at  $2\sigma$  ( $3\sigma$ ). The regions between the blue-solid line and the blue region are allowed by observed  ${}^6\text{Li}/{}^7\text{Li}$  abundance at  $2\sigma$ . The orange-solid lines (“Theoretical”) represent the yield value of the slepton when the BBN starts as a function of the mass difference. The colored regions are excluded for  ${}^6\text{Li}/{}^7\text{Li}$  (blue region; “ ${}^6\text{Li}/{}^7\text{Li}$  excluded”),  ${}^3\text{He}/\text{D}$  (red region; “ ${}^3\text{He}/\text{D}$  excluded”), and D/H (cyan region; “D/H excluded”), respectively. The shadowed and dotted regions are allowed by only  ${}^7\text{Li}/\text{H}$  ( $3\sigma$ ) and both  ${}^7\text{Li}/\text{H}$  ( $3\sigma$ ) and  ${}^6\text{Li}/{}^7\text{Li}$  ( $2\sigma$ ), respectively.

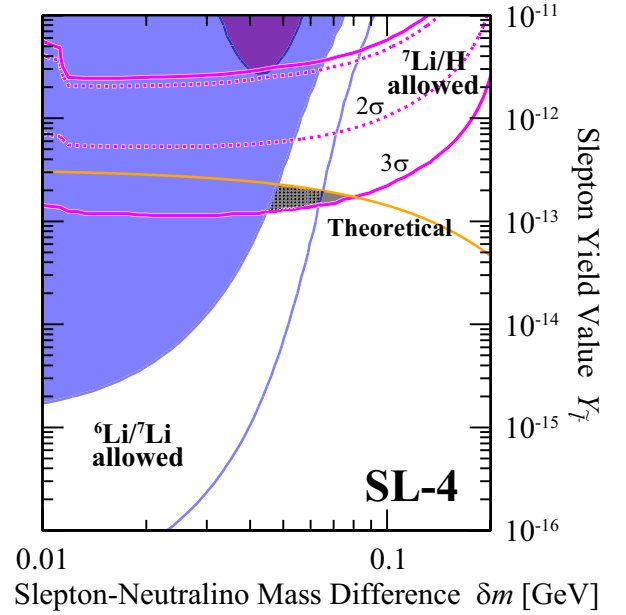
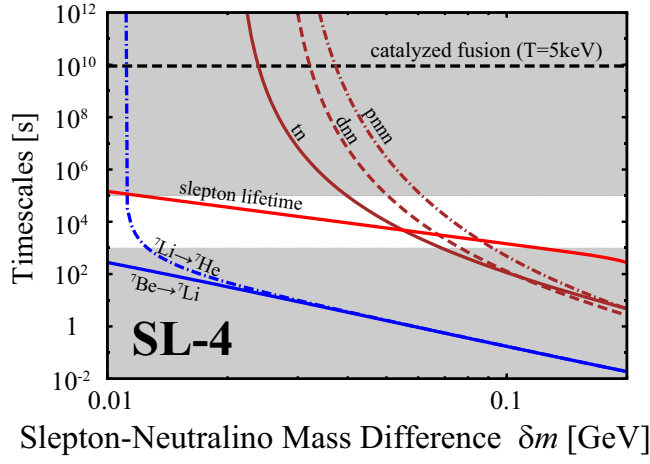
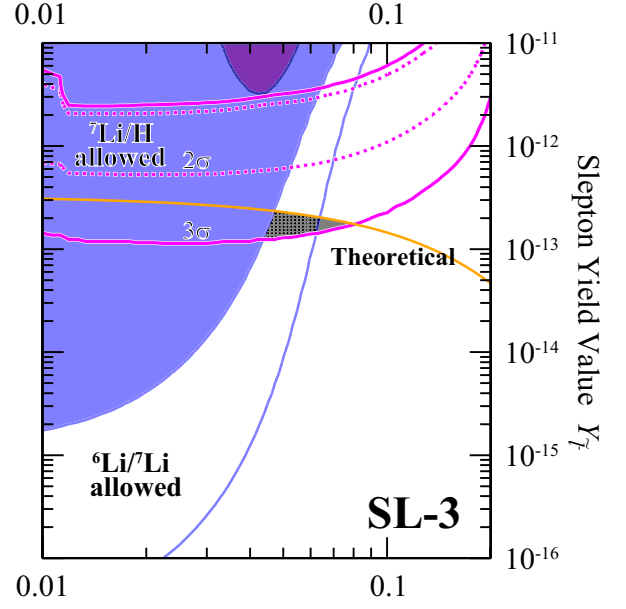
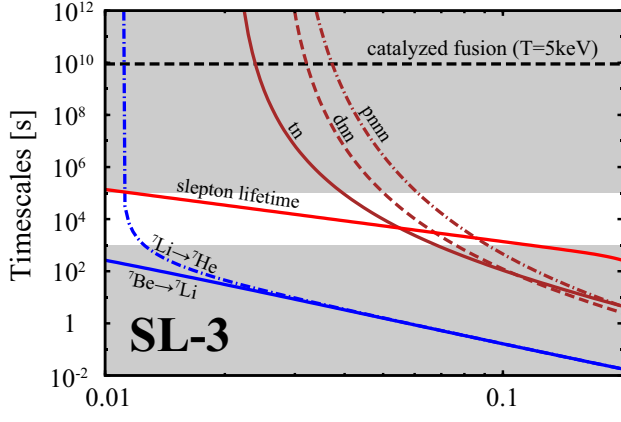


FIG. 6: The results at SL-3 (top panels) and SL-4 (bottom panels) are shown. The meanings of the lines and regions are same as those in the previous page.

### C. Bino-like neutralino LSP; large $\lambda$ - $\kappa$ region with small $\tan\beta$

We finally show the results in the third case where the neutralino LSP is bino-like with relatively large  $\lambda$ ,  $\kappa$  and small  $\tan\beta$ . In this case, the first term is dominant in the couplings Eqs. (8) and (9), and they hardly depend on the parameters,  $\lambda, \kappa, \tan\beta, \mu_{\text{eff}}, M_1$ , and  $M_2$ , since  $N_{1B}^2 \simeq 1$ . Therefore, we do not have to check the dependence on these parameters of the slepton lifetime and relevant timescales of the exotic BBN reactions (14) and (16) since they also do not depend on these parameters.

#### 1. Benchmark points

We take four reference points in the favored region for  $\tan\beta = 2$  as shown in Table V. Table VI shows the spectra and observables at these points. All the dimensionful values are represented in GeV. The top rows show input parameters and the middle rows show output spectra. Every points give the observed Higgs mass. As in the results of Sec. IV B, observed Higgs mass is obtained by virtue of large contribution of the tree terms. In this respect, the result is completely different from the case with bino-like neutralino in the MSSM, where the 1-loop contribution lifts up the Higgs mass.

In the bottom rows, we show relic density of the lightest neutralino, spin-independent cross section between the lightest neutralino and nucleon, the SUSY contribution to the muon anomalous magnetic moment, and the branching ratios of rare decays  $B_s \rightarrow \mu^+\mu^-$  and  $b \rightarrow s\gamma$ , from top to bottom. At each point, the dark matter relic density is in range of the measured value [4]. The spin-independent cross sections are about one order of magnitude smaller than those at points we chose in the previous section, and below the present experimental bound. The calculated values of  $\delta a_\mu$  at the points are below  $3\sigma$  range which is caused by small  $\tan\beta$ . For the branching ratio of  $B_s \rightarrow \mu^+\mu^-$  and  $b \rightarrow s\gamma$ , we obtained the values within  $1\sigma$  and  $2\sigma$ , respectively.

#### 2. BBN results at the benchmark points

The left panels in Fig. 7 show the slepton lifetime  $\tau_{\tilde{l}}$  (red-solid line; “slepton lifetime”), the timescales of the internal conversion processes (14a) (blue-solid line; “ ${}^7\text{Be} \rightarrow {}^7\text{Li}$ ”), (14b) (blue-dash-dotted line; “ ${}^7\text{Li} \rightarrow {}^7\text{He}$ ”), the  ${}^4\text{He}$  spallation processes (16a) (brown-solid line; “tn”), (16b) (brown-dashed line; “dnn”), and (16c) (brown-dash-dotted line; “pnnn”), as a function of the mass difference between the slepton NLSP and the neutralino LSP at BL-1, BL-2, BL-3, and BL-4 from top to bottom, respectively. The horizontal black-dashed line represents the timescale of the catalyzed fusion process (15) [19] at the temperature  $T = 5$  keV ( $5 \times 10^4$  s) when ( ${}^4\text{He} \tilde{l}^-$ ) is formed. In the right panels horizontal axis is

the mass difference between the slepton NLSP and the neutralino LSP, and vertical axis is the yield value of the slepton at the beginning of the BBN.

We show the allowed regions in the right panels of Fig. 7 which we obtain by comparing theoretical values to observational ones for light element abundances at BL-1, BL-2, BL-3, and BL-4 from top to bottom, respectively. The lines and regions are the same as those in the previous section. At BL-1, BL-2, and BL-3, we obtain allowed region only for  ${}^7\text{Li}/\text{H}$  ( $3\sigma$ ) while at BL-4, that for  ${}^6\text{Li}/{}^7\text{Li}$  ( $2\sigma$ ) is also obtained simultaneously.

At BL-2 and BL-3,  $\kappa$  and  $\lambda$  are small compared with those at BL-1, respectively. As was mentioned in the beginning of this section, the slepton lifetime and timescales of the internal conversion processes (14) and the  ${}^4\text{He}$  spallation processes (16) hardly depend on the NMSSM parameters. This is the reason why almost no difference exists among the results at BL-1, BL-2, and BL-3. The couplings  $G_{Lf}$  and  $G_{Rf}$  are large compared with those in the singlino-like LSP scenario, and hence the timescales of the internal conversion processes (14) and the  ${}^4\text{He}$  spallation processes (16) are one or two order of magnitude shorter than those in the singlino-like LSP scenario. Therefore, the observed abundance of  ${}^7\text{Li}/\text{H}$  is obtained in smaller slepton yield value compared with the singlino-like LSP scenarios, Fig. 3 and 6. In addition, the excluded regions by  ${}^3\text{He}/\text{D}$  and  $\text{D}/\text{H}$  lie downward compared to those of the singlino-LSP scenario (e.g., compare the results at SL-2 and BL-1). Indeed, the results at BL-1, BL-2, and BL-3 are almost same as the result in the MSSM, Fig. 3 in Ref. [10], where the same values for  $c_e, m_{\tilde{\chi}_1^0}, \sin\theta_f$  and CP-violating phase are used.

Only at BL-4, tiny flavor mixing exists. This result is similar to that in the MSSM, Fig. 4 (middle panel) in Ref. [11], where same values for  $c_e, m_{\tilde{\chi}_1^0}, \sin\theta_f$  and CP-violating phase are used.

TABLE V: Benchmark points on  $\lambda$ - $\kappa$  plane for  $\tan\beta = 2$ .

Parameters	BL-1	BL-2	BL-3	BL-4
$c_e$	0	0	0	$5 \times 10^{-11}$
$\lambda$	0.68	0.68	0.6	0.68
$\kappa$	0.32	0.2	0.32	0.32

TABLE VI: Spectra and observables at each point (see Tab. V). All the dimensionful values are shown in GeV. The top rows show input parameters. BL-1 and BL-4 give common results since we omit small flavor mixing of the slepton. The middle rows show output spectra. The bottom rows show relic density of the lightest neutralino, spin-independent cross section between the lightest neutralino and nucleon, the SUSY contribution to the muon anomalous magnetic moment, and the branching ratios of rare decays  $B_s \rightarrow \mu^+\mu^-$  and  $b \rightarrow s\gamma$ , and couplings Eqs. (8) and (9) from top to bottom.

Input	BL-1, BL-4	BL-2	BL-3
$M_2$	713.36	713.25	712.97
$A_t$	-1500.0	-1500.0	-1500.0
$m_{\tilde{L}_3}$	359.32	359.32	359.32
$m_{\tilde{E}_3}$	354.76	354.76	354.76
$m_{\tilde{Q}_3}$	1000.0	1000.0	1000.0
$\lambda$	0.6800	0.6800	0.6000
$\kappa$	0.3200	0.2000	0.3200
$A_\lambda$	1000.0	1480.0	1500.0
$A_\kappa$	-100.00	-100.00	-100.00
$\mu_{\text{eff}}$	900.00	900.00	900.00
$\tan\beta$	2.0000	2.0000	2.0000
Output			
$h_1^0$	125.23	126.51	124.35
$h_2^0$	844.57	552.89	960.06
$h_3^0$	1793.5	1983.6	2115.8
$a_1^0$	372.60	289.22	379.68
$a_2^0$	1792.3	1983.7	2114.5
$H^\pm$	1783.8	1974.3	2108.5
$\tilde{t}_1$	853.37	853.41	853.51
$\tilde{t}_2$	1132.1	1132.1	1132.2
$\tilde{\tau}_1$	350.10	350.10	350.10
$\tilde{\tau}_2$	367.13	367.13	367.13
$\tilde{\chi}_1^0$	350.00	350.00	350.00
$\tilde{\chi}_2^0$	696.36	534.28	697.51
$\tilde{\chi}_3^0$	842.69	699.36	906.34
$\tilde{\chi}_4^0$	908.00	909.78	914.24
$\tilde{\chi}_5^0$	944.68	934.66	984.08
$\Omega_{\tilde{\chi}_1^0} h^2$	0.11956	0.11964	0.11968
$\sigma_{\text{SI}}[\text{cm}^2]$	$3.6870 \times 10^{-46}$	$3.7874 \times 10^{-46}$	$3.7116 \times 10^{-46}$
$\delta a_\mu$	$1.3398 \times 10^{-10} (> 3\sigma)$	$1.3370 \times 10^{-10} (> 3\sigma)$	$1.3296 \times 10^{-10} (> 3\sigma)$
$\text{Br}(B_s^0 \rightarrow \mu^+\mu^-)$	$3.5381 \times 10^{-9} (1\sigma)$	$3.5382 \times 10^{-9} (1\sigma)$	$3.5383 \times 10^{-9} (1\sigma)$
$\text{Br}(b \rightarrow s\gamma)$	$3.1907 \times 10^{-4} (2\sigma)$	$3.1754 \times 10^{-4} (2\sigma)$	$3.1668 \times 10^{-4} (2\sigma)$
$G_{L\tau}/c_\tau$	0.15080	0.15080	0.15076
$G_{R\tau}/c_\tau$	0.40310	0.40310	0.40313
$G_{Le}/c_e$	0.15108	0.15108	0.15108
$G_{Re}/c_e$	0.40289	0.40289	0.40289

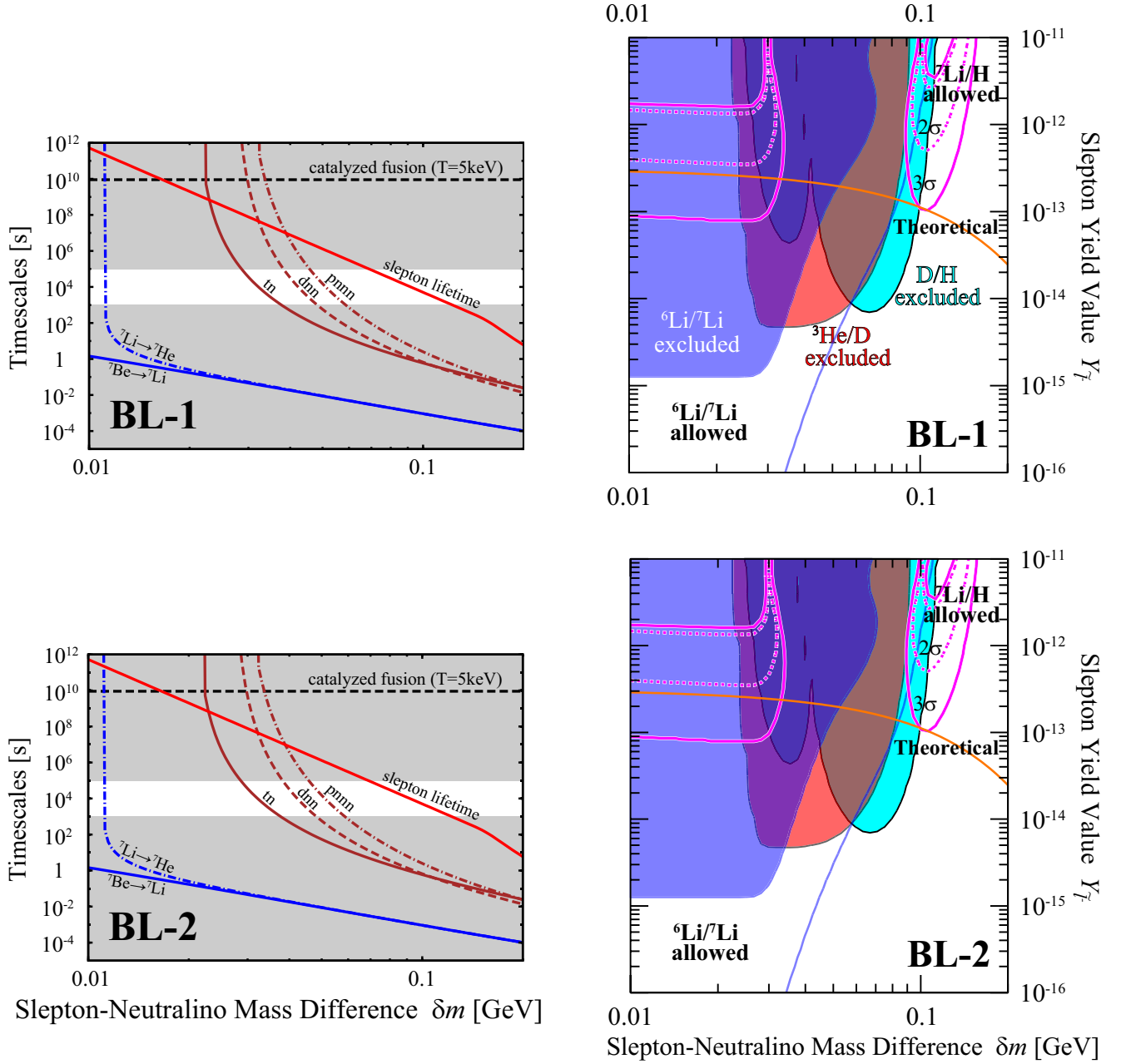


FIG. 7: The left panels show the slepton lifetime  $\tau_{\tilde{l}}$  (red-solid line; “slepton lifetime”), the timescales of the internal conversion processes, Eqs. (14a) (blue-solid line; “ ${}^7\text{Be} \rightarrow {}^7\text{Li}$ ”) and (14b) (blue-dash-dotted line; “ ${}^7\text{Li} \rightarrow {}^7\text{He}$ ”), the  ${}^4\text{He}$  spallation processes, Eqs. (16a) (brown-solid line; “tn”), (16b) (brown-dashed line; “dnn”), and (16c) (brown-dash-dotted line; “pnnn”), as a function of the mass difference between the slepton and the neutralino at BL-1 (top panel) and BL-2 (bottom panel). We also show the timescale of the catalyzed fusion (15) at the temperature  $T = 5 \text{ keV}$  ( $5 \times 10^4 \text{ s}$ ) when ( ${}^4\text{He} \tilde{l}^-$ ) is formed as horizontal black-dashed line. In the shaded regions, Eq. (17) is not satisfied. The right panels show the allowed regions from observational light element abundances on  $\delta m - Y_{\tilde{l}^-}$  plane at BL-1 (top panel) and BL-2 (bottom panel). The regions surrounded by magenta-dotted(-solid) lines are allowed by observed  ${}^7\text{Li}/\text{H}$  abundance at  $2\sigma$ ( $3\sigma$ ). The regions between the blue-solid line and the blue region are allowed by observed  ${}^6\text{Li}/{}^7\text{Li}$  abundance at  $2\sigma$ . The orange-solid lines (“Theoretical”) represent the yield value of the slepton when the BBN starts as a function of the mass difference. The colored regions are excluded for  ${}^6\text{Li}/{}^7\text{Li}$  (blue region; “ ${}^6\text{Li}/{}^7\text{Li}$  excluded”),  ${}^3\text{He}/\text{D}$  (red region; “ ${}^3\text{He}/\text{D}$  excluded”), and D/H (cyan region; “D/H excluded”), respectively. The shadowed and dotted regions are allowed by only  ${}^7\text{Li}/\text{H}$  ( $3\sigma$ ) and both  ${}^7\text{Li}/\text{H}$  ( $3\sigma$ ) and  ${}^6\text{Li}/{}^7\text{Li}$  ( $2\sigma$ ), respectively.

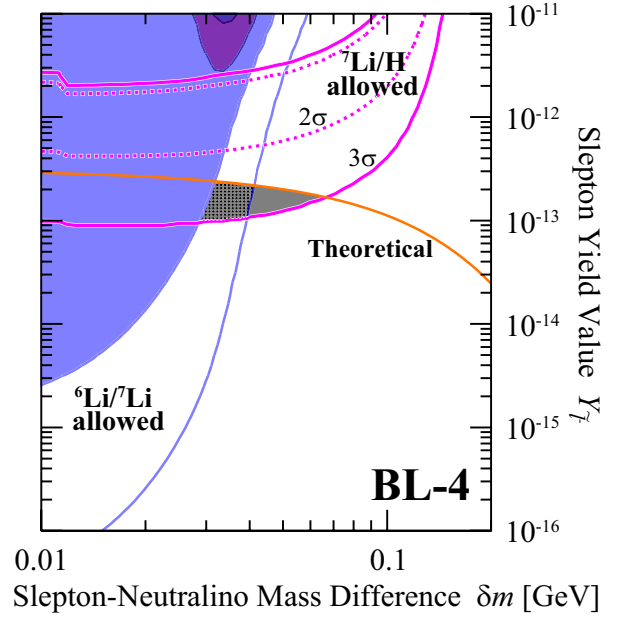
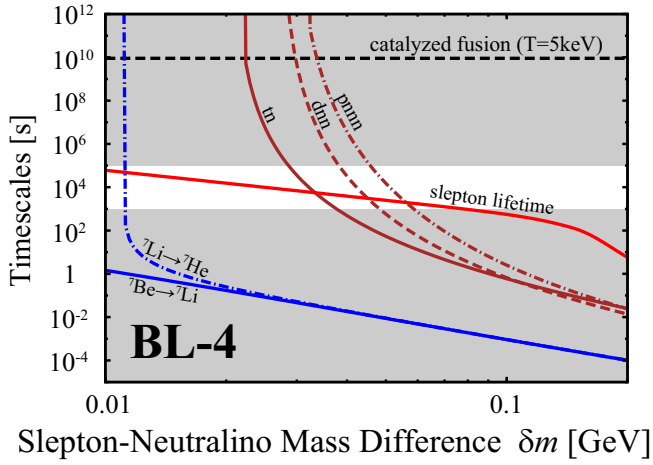
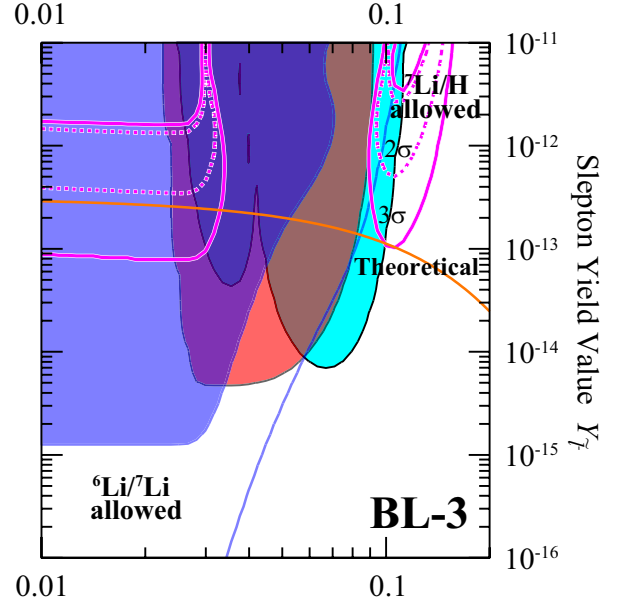
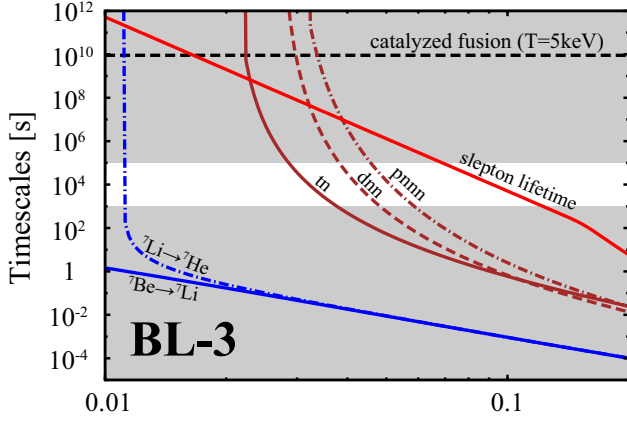


FIG. 7: The results at BL-3 (top panels) and BL-4 (bottom panels) are shown. The meanings of the lines and regions are same as those in the previous page.

## V. SUMMARY

The precise observations of the universe confirmed the presence of dark matter and raised a crucial question on its nature. Another possible problem is the discrepancy of the abundance of  ${}^7\text{Li}$  and  ${}^6\text{Li}$ . Models are attractive when they can account for these problems and at the same time are consistent with the observed mass of Higgs particle. We demonstrated that the NMSSM can be a candidate for such models.

We specifically considered the case where the neutralino is the stable LSP and the lightest slepton is the NLSP, and where the mass difference of the two is so tiny that the slepton becomes long-lived enough to survive until the time of the nucleosynthesis in the early universe. The sleptons interact with the synthesized nuclei and turn into the LSPs that stay until today as dark matter particles, altering the relic abundance of the light elements.

First, we searched for the benchmark sets of parameters that can successfully drive this scenario and simultaneously can reproduce the mass of Higgs particle within  $(125.6 \pm 3.0)\text{GeV}$ . Three cases of benchmark parameters are presented: (a) Singlino-like neutralino, small  $\lambda$ - $\kappa$  with large  $\tan\beta$ ; (b) Singlino-like neutralino, large  $\lambda$ - $\kappa$  with small  $\tan\beta$ ; and (c) Bino-like neutralino, large  $\lambda$ - $\kappa$  with small  $\tan\beta$ . We found the successful benchmark values of  $(c_e, \lambda, \kappa)$  in all the three cases. We confirmed that they lead to the permissible abundance of dark matter and are consistent with other experimental bounds as presented in Tables II, IV, and VI.

We then traced the BBN reaction network including the exotic nuclear reactions. We employed  $Y_{\tilde{l}^-}$  (slepton yield value)- $\delta m$  (LSP-NLSP mass difference) parameter plane to present the regions of parameters that can account for the observed abundance of light elements.

The results are illustrated in terms of timescales for the relevant exotic BBN reactions as follows. The slepton needs to be long-lived enough to form the bound state with  ${}^7\text{Be}$ , while the couplings  $G_{L,R\tau}$  should be large enough so that the internal conversion processes occur sufficiently. The slepton lifetime is thus subject to the lower bound. Meanwhile, the bound state of  $({}^4\text{He } \tilde{l}^-)$  accompanies other two relevant processes: one is the  ${}^4\text{He}$  spallation, and the other is the catalyzed fusion. These processes can readily overproduce the light elements and should be avoided, but suitable amount of  ${}^6\text{Li}$  production is favorable in order to account for its observed abundance. Of the two, the  ${}^4\text{He}$  spallation generally proceeds more efficiently and is prone to overproduction, but it can be avoided when the slepton has not too long lifetime and less of it forms a bound state with  ${}^4\text{He}$ . In ad-

dition, such lifetime can induce appropriate abundance of  ${}^6\text{Li}$  via catalyzed fusion as its observed abundance is tiny as explained around Eq. (32). Upper bound on the slepton lifetime is thus brought in. Combining the above arguments, we obtain an allowed window of the slepton lifetime.

In the case of (a) (Fig. 3), the specific relation between  $\lambda$  and  $\kappa$  is necessary to make the couplings  $G_{L,R\tau}$  large and thus to reduce  ${}^7\text{Be}$  by the internal conversion processes. Indeed, we tune the parameters  $\lambda$  and  $\kappa$  to make  $\mu_\kappa^2 - \mu_{\text{eff}}^2$  small and hence  $G_{L,R\tau}$  large at SS-1. We still need a sizable flavor mixing,  $c_e$ , in order to render the slepton lifetime short and thereby reduce the number of  $({}^4\text{He } \tilde{l}^-)$ . Thus we obtain the allowed region at SS-1. On the contrary, the flavor mixing  $c_e$  is small at SS-2 and hence the slepton lifetime becomes longer. Allowed region is thus shifted toward larger  $\delta m$ . The values of  $G_{L,R}$  become rapidly small outside the tuned parameter region of  $\lambda$  and  $\kappa$  so that the allowed region becomes small (SS-4). In the case of (b) (Fig. 6), the values of  $G_{L,R}$  are large due to large  $\lambda$  and  $\kappa$ , and thus the internal conversion processes occur efficiently. Suitable flavor mixings are also necessary as in the case of (a) to avoid the excessive amount of  $({}^4\text{He } \tilde{l}^-)$ . Otherwise, we may miss the allowed region (SL-2). In the case of (c) (Fig. 7), the couplings  $G_{L,R\tau}$  hardly depend on  $\lambda$  and  $\kappa$ , and thus the results are same as in the case of the MSSM.

We conclude that our scenario successfully works in the NMSSM and can simultaneously account for the abundance of dark matter, that of light elements, and the mass of Higgs particle. Since all the three cases we considered here are consistent to the present phenomenological bounds, they should be distinguished through the characteristic signals of accelerator experiments. Search for such signals are left for future works.

## Acknowledgments

The work of Y.K. was financially supported by the Sasakawa Scientific Research Grant from The Japan Science Society. This work was supported in part by the Grant-in-Aid for the Ministry of Education, Culture, Sports, Science, and Technology, Government of Japan, Nos. 21111006, 22244030, 23540327 (K.K.), No. 24740145 (M.K.), Nos. 24340044 and 25105009 (J.S.), No. 23740190 (T.S.), Nos. 23740208 and 25003345 (M.Y.), and by the Center for the Promotion of Integrated Science (CPIS) of Sokendai (1HB5804100) (K.K.).

[1] G. Aad *et al.* [ATLAS Collaboration], Phys. Lett. B **716**, 1 (2012) [arXiv:1207.7214 [hep-ex]].

[2] S. Chatrchyan *et al.* [CMS Collaboration], Phys. Lett. B **716**, 30 (2012) [arXiv:1207.7235 [hep-ex]].

- [3] C. L. Bennett *et al.* [WMAP Collaboration], *Astrophys. J. Suppl.* **208**, 20 (2013) [arXiv:1212.5225 [astro-ph.CO]].
- [4] P. A. R. Ade *et al.* [Planck Collaboration], arXiv:1303.5076 [astro-ph.CO].
- [5] J. E. Kim and H. P. Nilles, *Phys. Lett. B* **138**, 150 (1984).
- [6] T. Jittoh, J. Sato, T. Shimomura and M. Yamanaka, *Phys. Rev. D* **73**, 055009 (2006) [Erratum-ibid. **D 87**, 019901 (2013)] [hep-ph/0512197].
- [7] T. Jittoh, K. Kohri, M. Koike, J. Sato, T. Shimomura and M. Yamanaka, *Phys. Rev. D* **76**, 125023 (2007) [arXiv:0704.2914 [hep-ph]].
- [8] T. Jittoh, K. Kohri, M. Koike, J. Sato, T. Shimomura and M. Yamanaka, *Phys. Rev. D* **78**, 055007 (2008) [arXiv:0805.3389 [hep-ph]].
- [9] T. Jittoh, K. Kohri, M. Koike, J. Sato, T. Shimomura and M. Yamanaka, *Phys. Rev. D* **82**, 115030 (2010) [arXiv:1001.1217 [hep-ph]].
- [10] T. Jittoh, K. Kohri, M. Koike, J. Sato, K. Sugai, M. Yamanaka and K. Yazaki, *Phys. Rev. D* **84**, 035008 (2011) [arXiv:1105.1431 [hep-ph]].
- [11] K. Kohri, S. Ohta, J. Sato, T. Shimomura and M. Yamanaka, *Phys. Rev. D* **86**, 095024 (2012) [arXiv:1208.5533 [hep-ph]].
- [12] J. Melendez and I. Ramirez, *Astrophys. J.* **615** (2004) L33.
- [13] M. Asplund, D. L. Lambert, P. E. Nissen, F. Primas and V. V. Smith, *Astrophys. J.* **644** (2006) 229 [arXiv:astro-ph/0510636].
- [14] Y. Konishi, S. Ohta, J. Sato, T. Shimomura, K. Sugai and M. Yamanaka, arXiv:1309.2067 [hep-ph].
- [15] K. Griest and D. Seckel, *Phys. Rev. D* **43** (1991) 3191.
- [16] K. Kohri and F. Takayama, *Phys. Rev. D* **76**, 063507 (2007) [hep-ph/0605243].
- [17] C. Bird, K. Koopmans and M. Pospelov, *Phys. Rev. D* **78**, 083010 (2008) [arXiv:hep-ph/0703096].
- [18] M. Pospelov, *Phys. Rev. Lett.* **98**, 231301 (2007) [arXiv:hep-ph/0605215].
- [19] K. Hamaguchi, T. Hatsuda, M. Kamimura, Y. Kino and T. T. Yanagida, *Phys. Lett. B* **650** (2007) 268 [arXiv:hep-ph/0702274].
- [20] M. Kawasaki, K. Kohri and T. Moroi, *Phys. Lett. B* **649**, 436 (2007) [hep-ph/0703122].
- [21] M. Muhlleitner, A. Djouadi and Y. Mambrini, *Comput. Phys. Commun.* **168** (2005) 46 [hep-ph/0311167].
- [22] U. Ellwanger, J. F. Gunion and C. Hugonie, *JHEP* **0502** (2005) 066 [hep-ph/0406215].
- [23] G. Belanger, F. Boudjema, C. Hugonie, A. Pukhov and A. Semenov, *JCAP* **0509** (2005) 001 [hep-ph/0505142].
- [24] U. Ellwanger and C. Hugonie, *Comput. Phys. Commun.* **175** (2006) 290 [hep-ph/0508022].
- [25] U. Ellwanger and C. Hugonie, *Comput. Phys. Commun.* **177** (2007) 399 [hep-ph/0612134].
- [26] S. F. King, M. Muhlleitner and R. Nevzorov, *Nucl. Phys. B* **860** (2012) 207 [arXiv:1201.2671 [hep-ph]].
- [27] G. Belanger, F. Boudjema, A. Pukhov and A. Semenov, *Comput. Phys. Commun.* **185** (2014) 960 [arXiv:1305.0237 [hep-ph]].
- [28] [CMS Collaboration], CMS-PAS-HIG-13-005.
- [29] [ATLAS Collaboration], ATLAS-CONF-2013-014.
- [30] B. C. Allanach, *eConf C* **010630**, P319 (2001) [hep-ph/0110227].
- [31] A. Djouadi, hep-ph/0211357.
- [32] B. C. Allanach, S. Kraml and W. Porod, *JHEP* **0303**, 016 (2003) [hep-ph/0302102].
- [33] B. C. Allanach, A. Djouadi, J. L. Kneur, W. Porod and P. Slavich, *JHEP* **0409**, 044 (2004) [hep-ph/0406166].
- [34] J. -J. Cao, Z. -X. Heng, J. M. Yang, Y. -M. Zhang and J. -Y. Zhu, *JHEP* **1203** (2012) 086 [arXiv:1202.5821 [hep-ph]].
- [35] M. Pettini, B. J. Zych, M. T. Murphy, A. Lewis and C. C. Steidel, *MNRAS*, **391** (2008) 1499.
- [36] J. Geiss and G. Gloeckler, *Space Science Reviews* **106**, 3 (2003).
- [37] M. Pettini and R. Cooke, *Mon. Not. Roy. Astron. Soc.* **425**, 2477 (2012) [arXiv:1205.3785 [astro-ph.CO]].
- [38] R. Cooke, M. Pettini, R. A. Jorgenson, M. T. Murphy and C. C. Steidel, arXiv:1308.3240 [astro-ph.CO].
- [39] G. W. Bennett *et al.* [Muon G-2 Collaboration], *Phys. Rev. D* **73** (2006) 072003 [hep-ex/0602035].
- [40] M. Davier, A. Hoecker, B. Malaescu and Z. Zhang, *Eur. Phys. J. C* **71** (2011) 1515 [Erratum-ibid. **C 72** (2012) 1874] [arXiv:1010.4180 [hep-ph]].
- [41] K. Hagiwara, R. Liao, A. D. Martin, D. Nomura and T. Teubner, *J. Phys. G* **38** (2011) 085003 [arXiv:1105.3149 [hep-ph]].
- [42] S. Chatrchyan *et al.* [CMS Collaboration], *Phys. Rev. Lett.* **111** (2013) 101804 [arXiv:1307.5025 [hep-ex]].
- [43] RAaaj *et al.* [LHCb Collaboration], *Phys. Rev. Lett.* **111** (2013) 101805 [arXiv:1307.5024 [hep-ex]].
- [44] Y. Amhis *et al.* [Heavy Flavor Averaging Group Collaboration], arXiv:1207.1158 [hep-ex].
- [45] D. S. Akerib *et al.* [LUX Collaboration], arXiv:1310.8214 [astro-ph.CO].